Contrasting mechanisms of magma fragmentation during coeval magmatic and hydromagmatic activity: The Hverfjall Fires fissure eruption, Iceland

E.J. Liu[*1], K.V. Cashman[2], A.C. Rust[2], & A., Höskuldsson[3]

[1]Department of Earth Sciences, University of Cambridge, Downing Street, Cambridge, CB2 3EQ, UK.

[2]School of Earth Sciences, University of Bristol, Wills Memorial Building, Bristol, BS81RJ, UK.

[3]Institute of Earth Sciences, University of Iceland, Reykjavik, Iceland.

*Corresponding author: EJL (ejl54@cam.ac.uk)

Abstract

Growing evidence for significant magmatic vesiculation prior to magma-water interaction (MWI) has brought into question the use of 'diagnostic' features, such as low vesicularities and blocky morphologies, to identify hydromagmatic pyroclasts. We address this question by quantifying co-variations in particle size, shape and texture in both magmatic and hydromagmatic deposits from the Hverfjall Fires fissure eruption, Iceland. Overlapping vesicularity and bubble number density distributions measured in rapidly quenched magmatic and hydromagmatic pyroclasts indicate a shared initial history of bubble nucleation and growth, with substantial vesiculation prior to MWI. Hydromagmatic fragmentation occurred principally by brittle mechanisms, where the length-scale and geometry of fracturing was controlled by the bubble population. This suggests that the elevated fragmentation efficiency of hydromagmatic deposits is driven, at least in part, by brittle disintegration of vesicular pyroclasts due to high thermal stress generated during rapid cooling. In this way, the shape and size distributions of hydromagmatic pyroclasts, both critical input parameters for ash dispersion models, are strongly influenced by the dynamics of vesiculation prior to MWI. This

result underlines the need to analyse multiple grain-size fractions to characterise the balance between magmatic and hydromagmatic processes.

During the Hverfjall Fires eruption, the external water supply was sufficient to maintain MWI throughout the eruption, with no evidence for progressive exhaustion of a water reservoir. We suggest that both the longevity and the spatial distribution of MWI was determined by the pre-existing regional hydrology, and represents continuous interaction between a propagating dike and a strong groundwater flow system hosted within permeable basalt lavas.

1. Introduction

Hydromagmatic activity is characterised by much greater fragmentation efficiencies (i.e. producing more fine-grained ash), and therefore more widespread tephra deposition, than equivalent magmatic eruptions (e.g., Walker & Croasdale 1971; Walker 1973; Houghton & Nairn 1991; Houghton et al. 1999; Mastin et al. 2004; Németh & Cronin 2011; Németh et al. 2012; Van Otterloo et al. 2013; Gjerløw et al. 2015; Liu et al. 2015b). Anticipating the unique hazards of eruptions involving explosive magma-water interaction (MWI; Cioni et al. 1992; Mastin et al. 2004; Zimanowski et al. 2003; Németh & Cronin 2011; Dellino et al. 2012; Liu et al. 2015b) requires that 'wet' vs. 'dry' eruptions can be determined from the deposit characteristics of past eruptions. Wet vs. dry deposits are typically distinguished on the basis of both sedimentological characteristics (e.g., Lorenz, 1974; Chough and Sohn, 1990; Cole et al., 2001; Solgevik et al., 2007) and the nature of the constituent ash particles. Of the latter, small grain sizes and ash with blocky morphologies and low vesicularities are often taken as diagnostic of hydromagmatic eruptions (e.g., Heiken and Wohletz, 1985; Büttner et al., 1999; Büttner et al., 2002). Increasing evidence suggests, however, that the boundary between magmatic and hydromagmatic deposits may be blurred, and that magmatic and hydromagmatic

fragmentation styles often occur simultaneously (Cioni et al., 1992; Graettinger et al., 2013; Murtagh and White, 2013; Liu et al., 2015a; White and Valentine, 2016). A more complete understanding of the controls on hydromagmatic fragmentation requires comparison of the products of hydromagmatic and magmatic eruptions to identify not only their differences but also their shared characteristics.

Contrasting fragmentation efficiencies between wet and dry eruptions are highlighted by compilations of grain size data for mafic deposits (e.g., Walker and Croasdale, 1971; Walker, 1971; Houghton and Hackett, 1984; Cole et al., 2001; Liu et al., 2015a). In contrast to those mafic eruptions in which coarse inertial fragmentation is driven by rapid vesiculation (Mangan and Cashman, 1996; Parfitt, 1998; Mangan et al., 2014), extensive melt fragmentation during MWI reflects brittle breakage in response to high rates of thermal to mechanical energy transfer (Peckover et al., 1973; Colgate and Sigurgeirsson, 1973; Sheridan and Wohletz, 1983; Kokelaar, 1986; Wohletz, 1986; Zimanowski et al., 1991; Zimanowski et al., 1997; Büttner et al., 2002; Van Otterloo et al., 2015). Here, brittle fragmentation is driven by rapid vaporisation and expansion of external water ('steam explosivity'), and/or thermal stress created by rapid cooling and contraction of pyroclasts.

The physical state of magma at the point of fragmentation can be inferred from primary vesicle (and crystal) textures (e.g., Klug and Cashman, 1994; Cashman and Blundy, 2000; Cashman et al., 2004; Lautze and Houghton, 2007; Wright et al., 2012; Rust and Cashman, 2011; Stovall et al., 2011, 2012; Alfano et al., 2011; Murtagh and White, 2013; Cioni et al., 2014). In the products of mafic magmatic eruptions, only rapidly-cooled clasts, such as ash or the quenched outer rims of lapilli, closely approximate the primary bubble population at the time of fragmentation. The products of hydromagmatic eruptions should also quench rapidly, and thus preserve fragmentation information. Vesicle measurements are comparatively scarce for mafic hydromagmatic deposits, however, and most of these data are for eruptions involving

80 interaction with surface water. Overall, the products of these ‘Surtseyan’ eruptions span an
81 exceptionally broad range of vesicularities, from 5 to 90% (Fig. 1). These data show that whilst
82 low vesicularities may be a feature of deep-seated diatremes (e.g., Ross and White, 2012), the
83 vesicularity ranges of Surtseyan-style eruptions and Hawaiian lava fountains overlap between
84 40% and 70% (e.g., Stovall et al., 2011). In other words, moderate to high vesicularity is not
85 sufficient to rule out a hydromagmatic origin. Furthermore, the range of bubble number
86 densities (BNDs) is also comparable between magmatic and hydromagmatic mafic deposits
87 and is independent of clast vesicularity; these similarities suggest that magma involved in both
88 eruption styles shares a common ascent (decompression) path. Most importantly, the high
89 BNDs and vesicularities of many hydromagmatic pyroclasts indicate substantial magmatic
90 vesiculation prior to MWI (e.g., Mastin et al., 2004).

91 Explosive hydromagmatic activity includes intermittent steam-laden tephra jets and/or
92 variably water-saturated base surges (e.g., Þórarinsson, 1967; Moore, 1967; Chough and Sohn,
93 1990; Nemeth et al., 2006). Base surges are turbulent, low-particle concentration density
94 currents that spread away from the base of a collapsing debris-laden eruption column (Moore
95 1967; Waters & Fisher 1971; Fisher 1983; Németh et al. 2006). Variations in hydromagmatic
96 eruptive style are controlled by complex interactions between intrinsic (magmatic) and
97 extrinsic (environmental) factors that determine the efficiency of thermal to mechanical energy
98 transfer, including (a) the magma-water ratio, (b) the depth of MWI, (c) the properties of the
99 host substrate, and (d) the geometry of the conduit (Wohletz and Sheridan, 1983; Wohletz,
100 1983; Aranda-Gomez and Luhr, 1996; Sohn, 1996; Solgevik et al., 2007; Pedrazzi et al., 2013).
101 The interplay between magmatic vesiculation and the dynamics of MWI has important
102 implications for fragmentation mechanisms, but is not yet fully explored in existing models of
103 hydromagmatism (Murtagh, et al., 2011; Murtagh and White, 2013; Liu et al., 2015a). To what

extent do changes in the conditions of magma ascent (i.e., ascent rate, volatile content and degree of vesiculation) influence the nature of how magma and water interact?

In this study we explore the effect of vesiculation *prior* to MWI on fragmentation by comparing coeval magmatic and hydromagmatic deposits from the 2500 BP Hverfjall Fires basaltic fissure eruption, Iceland. As all vents shared the same initial magma composition and feeder system, differences in pre-fragmentation magma texture are inferred to have been minimal and we interpret differences in the morphology and textures of pyroclasts as recording the effects of fragmentation under different near-surface conditions. The excellent preservation of these largely unaltered/non-palagonitised deposits provides an opportunity to investigate not only the role of water on the efficiency and mechanism of magma fragmentation, but also the conditions under which MWI took place, including the physical state of the magma. By exploring co-variation in pyroclast morphology, vesicle texture, and density over the full range of available grain sizes and stratigraphic exposure, we identify the controls on the length-scale and geometry of hydromagmatic fragmentation, and consequently the physical mechanisms of fine ash generation. Furthermore, we consider the extent to which variations in pyroclast properties and deposit architecture reflect changes in either the conditions of magma ascent or the environment of MWI.

2. Geological setting

The Krafla Volcanic System (KVS; Fig. 2a) is located in Iceland's Northern Volcanic Zone, and comprises a central caldera with a transecting fissure system distributed over an area of 900 km^3 (Thordarson and Höskuldsson, 2008). Rifting in the KVS is controlled by the regional stress field, with fractures and fissures striking N to NNE perpendicular to the extensional stress direction (Hjartardottir et al., 2012).

The Mývatn region lies within the KVS and comprises a shallow lake-filled depression, bounded to the west by low Plio-Pleistocene basalt ridges and to the east by the young Námafjall hyaloclastite ridge (Þórarinsson, 1979). Postglacial volcanic activity in the region commenced ~6000 years ago with the Ludent Fires, during which explosive activity formed the Ludent tuff ring. Subsequently, the Mývatn area was covered by the extensive Older Laxáhraun pahoehoe lava flow (~3.8 ka) that originated from a shield volcano 25 km SE of Mývatn. This lava flow dammed the western drainage outflow from the depression towards Laxádalur, forming proto-Lake Mývatn (Fig. 2b; Einarsson, 1982).

Following a long period of volcanic quiescence in the Mývatn region, activation of a ~50 km-long fissure segment within the Krafla volcanic zone initiated the Hverfjall Fires ~2500 years ago (Þórarinsson, 1952; Saemundsson, 1991; Mattsson and Höskuldsson, 2011). Effusive activity occurred intermittently along the NNE-SSW aligned fissure, which extended both north and south of the central Krafla caldera (Fig. 2; Saemundsson, 1991). Most of the activity was concentrated at the southernmost tip of the fissure, in Mývatn, where explosive activity localised at two coeval fissure vents that formed a (magmatic) scoria cone within the composite Jarðbaðshólar cone complex (hereafter referred to singularly as Jarðbaðshólar for simplicity) and the (hydromagmatic) Hverfjall tuff ring (Mattsson and Höskuldsson, 2011). To avoid confusion in terminology, all references made to the 'Hverfjall vent' refer to the hydromagmatic vent and associated deposits, whilst the full name of the Hverfjall Fires is used when referring to the eruptive episode in its entirety.

The Threngslaborgir-Ludentsborgir cone row, extending south from the Hverfjall tuff ring, formed during a subsequent fissure eruption dated to ~2.1 ka. This eruption also fed the Younger Laxáhraun lava flows, which cover much of the area surrounding Lake Mývatn (Þórarinsson, 1952). Interaction between the Younger Laxáhraun lavas and the proto-Lake Mývatn modified the shape of the lake basin to its present day form, extending it northwards

153 to form the northern basin (Fig. 2b). Two major rifting episodes have taken place in the KVS
154 in historical times: the 1724–29 Mývatn Fires and the 1975–84 Krafla Fires (Þórarinsson, 1952;
155 Saemundsson, 1991).

156 The spatial distribution of the Hverfjall Fires deposits along the entire length of the
157 fissure was mapped in detail by Saemundsson (1991), and the deposits in the Mývatn region
158 later re-visited by Mattsson and Höskuldsson (2011). Most extensive are distal airfall tephra
159 deposits from the initial eruptive phase of the Hverfjall hydromagmatic vent, which are found
160 at distances of ≤ ~20 km. Isopach contours for this deposit, which also include thickness
161 measurements of subsequence base surge deposits from Hverfjall, are elongated to the NNE
162 and SSW (Fig. 2b; Saemundsson, 1991; Mattsson and Höskuldsson, 2011). Interbedded
163 magmatic and hydromagmatic deposits indicate that the Hverfjall vent and at least one vent
164 within the Jarðbaðshólar cone complex were active simultaneously. A previous study
165 suggested that magmatic activity at Jarðbaðshólar began after the onset of hydromagmatic
166 activity at Hverfjall, with the onset of activity at Jarðbaðshólar (closer to the inferred source in
167 the Krafla central caldera) and the consequent reduction in magma supply rate to the Hverfjall
168 vent, invoked to explain a temporal change in hydromagmatic eruptive style from fall-
169 dominated to surge-dominated deposition (Mattsson and Hoskuldsson, 2011).

170 Although generally referred to as a tuff ring, the Hverfjall edifice has morphological
171 properties transitional between those typical of tuff cones and tuff rings (Fig. 3a; Wohletz and
172 Sheridan, 1983; Sohn, 2006; White and Ross, 2011; Table S1). The low slope angle (18˚
173 maximum; 15˚ average) and the low height/crater rim ratio (0.125) are well within the
174 characteristic ranges of tuff rings (White and Ross, 2011; and references therein). However,
175 the total height of the edifice (125 m maximum) is substantially greater than typically observed
176 in tuff rings (< 50 m) and is instead more consistent with those of consolidated tuff cones
177 (White and Ross, 2011). Similarly ‘over-sized’ tuff rings and cones have been observed in

178 Hawaii (Honolulu Formation) and the Galapagos, but always in coastal littoral settings where
179 the intrusion of seawater into highly permeable basalt lavas provides a sustained source of
180 water (Lorenz, 2003). This association suggests that water supply is important and that regional
181 hydrology has a strong control on the dynamics of MWI and the resulting landforms (e.g.,
182 Sohn, 1996; Lorenz, 2003).

183 Hydromagmatic activity at the Hverfjall vent has been attributed to interaction with
184 surface water (Mattsson and Höskuldsson, 2011). Yet the absence of lake sediments beneath
185 even the most proximal hydromagmatic deposits (which also preserve terrestrial tree moulds;
186 Einarsson, 1953; Thorarinsson, 1962) raises the question of whether the spatial extent of proto-
187 Lake Mývatn extended as far as the Hverfjall tuff ring. Furthermore, the lack of field evidence
188 for a late-stage transition to 'dry' magmatic activity, as is commonly observed for other
189 hydromagmatic eruptions (e.g., Capelas, Azores; Solgevik et al. 2007; El Caracol, Mexico;
190 Kshirsagar et al. 2016; Surtsey, Iceland; Þórarinsson, 1967; Hunga Ha'apai, Tonga, Vaughan
191 & Webley 2010), suggests a near-continuous water supply sufficient to maintain MWI
192 throughout the eruption. This continuity in hydromagmatic activity is inconsistent with a sub-
193 lacustrine eruption. The present Lake Mývatn, which has been further impounded by
194 subsequent eruptions, has a maximum depth of only four metres and therefore offers only a
195 limited reservoir of external water. Indeed, water influx into Lake Mývatn is supplied almost
196 entirely by groundwater at a rate of ~30 m^3s^{-1} (Kristmannsdóttir and Ármannsson, 2004).
197 Below we suggest that the hydromagmatic activity at the Hverfjall vent was fuelled by an
198 actively replenished groundwater source.
199

200 **3. Methods**

201 **3.1 Samples**

Fieldwork was undertaken in 2013 and 2014. GPS coordinates and thickness data for all locations where observations were made and/or samples were collected are listed in the supplementary materials (Fig. 2; Table S2, supplementary information). The deposits of the Hverfjall Fires are easily identifiable in the field as they are stratigraphically above the widespread silicic Hekla-3 (H3) marker bed (Fig. 3b; Saemundsson, 1991). Samples from six locations – four hydromagmatic and two magmatic – were selected for detailed morphological and textural analysis (Table 1). All hydromagmatic samples are from the unconsolidated basal fall unit collected at different distances from the Hverfjall vent: they represent the opening phase of hydromagmatic activity. Subsequent surge deposits are indurated and partially palagonised, precluding measurements of individual particle properties or deposit grain size distributions. Magmatic samples are from quarried exposures through the scoria cone edifice, and the surrounding tephra blanket up to a distance of 1.3 km from the vent. With the exception of one locality (Q3), all sampled deposits clearly overlie H3 (± hydromagmatic units) and are therefore unequivocally linked to the Hverfjall Fires eruptive episode, rather than to earlier activity within the Jarðbaðshólar cone complex.

3.2 Granulometry

Grain size distributions (GSDs) were measured for all twenty-three hydromagmatic basal fall deposit sample locations (1.5 km to 19 km from the Hverfjall vent) and six magmatic deposits (0.2 km to 1.3 km from the Jarðbaðshólar vent active during the Fires). Ash samples were cleaned in an ultrasonic bath for 3–5 minutes and dried overnight at 80˚C. Dried samples were sieved manually in ½ phi (φ) intervals from -3φ to >5φ (8 to <0.032 mm; $\varphi = -\log_2 d$, where d = particle diameter in mm). For size fractions >3φ, disposable sieve meshes were used to minimise contamination between samples. Grain size distributions of sample splits comprising particles >2φ were also measured by laser diffraction from a wet dispersion (~2 g of sample

dispersed in 500 ml MilliQ purified and deionised water) using a Malvern Mastersizer 2000 at the University of Bristol, UK. Volumetric size distributions obtained from laser diffraction were converted to mass distributions assuming a constant density, and merged with sieve data using an overlap between 2φ and 3φ (125–250 μm; e.g., Eychenne et al., 2012). For the coarse scoria lapilli deposit at site Q1, the major and minor axes of 100 clasts < –5φ (> 32 mm) were measured in the field over a known area. These measurements were converted to mass assuming ellipsoidal clasts (where the intermediate and short axes were assumed to be equal) and a density of 700 kg m^{-3} (Fig. S3, supplementary information), binned in φ intervals (according to the intermediate particle axis), and merged with sieve data using an overlap between –4φ and –5φ (16–32 mm). Note that the GSD generated by this combined approach still does not include the very largest bombs, which are several tens of centimetres in length, as they could not be statistically sampled within the measurement area.

The Total Grain Size Distribution (TGSD) of the hydromagmatic basal fall deposit (not including overlying surge units) was estimated by weighting the GSDs at individual locations by the deposit volume contained between their enclosing isopachs (Murrow et al., 1980; Sparks et al., 1981). Although thickness measurements are numerous and widely distributed, the limited spatial distribution of the twenty-three locations with corresponding GSDs precludes a robust Voronoi tessellation for TGSD weighting (e.g., Bonadonna and Houghton, 2005; Bonadonna et al., 2015). Additionally, as the isopach map of Mattsson and Höskuldsson (2011; Fig. 2b) includes both fall and base surge deposits, TGSD estimates of the fall deposit alone required that we deconvolve the thinning behaviour of the fall and surge deposits (Fig. 4a; Table S2, supplementary information). Thinning of the total deposit is well-described by two straight-line segments on a semi-log plot of thickness versus $(\text{isopach area})^{1/2}$ (Fig. 4b; Pyle, 1989; Fierstein and Nathenson, 1992). Thinning of the fall deposit alone, however, can be

approximated by a single straight-line segment (Fig. 4b), which we use to calculate TGSD. Detailed methods are presented in Appendix 1 (supplementary information).

Bulk volumes of hydromagmatic deposits were calculated by integrating beneath both single-segment (basal fall unit only) and two-segment (fall and surge units) thinning relationships using AshCalc software (Fig. 4b; Daggitt et al., 2014), according to the method of Fierstein and Nathenson (1992). The uncertainties on the calculated volumes are estimated conservatively to be ~10% (Engwell et al., 2013); compaction and erosion are not accounted for. The volume of the cone edifice was calculated geometrically by approximating the morphology as two polygonal frustrums, with dimensions measured from GoogleEarth imagery and cross-sectional profiles (Fig. S1, supplementary information).

3.3 Image acquisition

Sieved size fractions (-2φ to >5φ; equivalent to 4 to <0.032 mm) were mounted separately in epoxy grain mounts, ground and polished, then carbon-coated and analysed at the University of Bristol using a Hitachi S-3500N scanning electron microscope (SEM) operating in backscattered electron (BSE) mode. BSE-SEM image mosaics of 20–40 images were acquired for each sample size fraction using a working distance of ~18.0 mm (z = 20 mm) and a 15kV accelerating voltage. The acquisition magnification was optimised for each grain-size fraction following Liu et al. (2015a) to ensure that the pixel density of each particle remained comparable between images of different size fractions (and above the critical pixel density of ~1000 pxls). Additional image mosaics of individual clasts (nineteen clasts in the 1–2 mm size fraction, one clast in the 2–4 mm size fraction, and the quenched rim of one 16–32 mm lapillus) were obtained at magnifications of either x100 or x250 (equivalent to resolutions of 555 pixels/mm and 1953 pixels/mm, respectively) for textural quantification.

3.4 Componentry

Using BSE-SEM image mosaics, >200 ash particles per sample size fraction were manually categorised into component classes using criteria related to the particle outline, bubble texture, crystal texture, and juvenile/non-juvenile character. The minimum sample size of 200 particles was defined by a sensitivity analysis in which we calculated the relative proportions of each component in randomly-generated subsamples of progressively larger size (from 1 to the total size of the dataset) and identified the sample size above which the variation in componentry became negligible (Fig. S2, supplementary information).

Total componentry distributions (TCDs) were determined for both hydromagmatic (basal fall only) and magmatic deposits by averaging the proportions of each ash component across all samples at each grain size, and weighting the contribution of each grain-size fraction according to the total grain size distribution (TGSD). This approach requires that (a) the variation in componentry between samples from different locations is small with respect to the variation between grain sizes, and (b) component proportions remain constant for all size fractions >5φ and <0φ, as demonstrated in Section 5.2. For the magmatic Jarðbaðshólar deposit, where a TGSD has not been determined, each grain size fraction is weighted based on a proximal grain size distribution from site Q1 (Fig. 2). This grain size distribution does not account for clast sizes larger than -5φ (32 mm); incorporation of larger size fractions would skew the distribution further towards larger grain sizes but would have little effect on the TCD, as all size fractions greater than 0φ are dominated by a single component class.

3.5 Density measurements

Variations in particle density over the full range of available size fractions were determined for four samples (sites 2.3, 9.3, 7.5, Q1; Table 1). For particles >–3φ (<8 mm), the average particle density in each grain-size fraction was determined by water pycnometry, using a 0.5 dm^3 boro-

silicate pycnometer, de-ionised water, and 1 g of sample per measurement (following the method of Eychenne et al., 2012). Measurements were repeated three times, and the resulting densities averaged. Average particle densities within individual size fractions are reproducible, with standard deviations generally <50 kg m^{-3}. Densities of individual lapilli within the –3φ (8–16 mm) size fraction were calculated from measurements of clast weight in air and in water, wrapped in Parafilm wax paper (e.g., Houghton and Wilson, 1989). As shown in Figure S3 (supplementary information), our sample size of 45 measurements is sufficient to characterise the density distribution.

3.6 Textural analysis

Vesicle textures were quantified from 2D BSE-SEM image mosaics using ImageJ image processing software. BSE-SEM images were manually cleaned to remove particles from inside vesicles, and thresholded to separate vesicles, crystals and glass. Vesicle areas were converted into circular equivalent diameters (EqD = $2\sqrt{\pi A}$, where A is the measured vesicle area), and binned into lognormal size classes in ½φ increments. The use of lognormal size bins (instead of geometric bins; e.g., Sahagian and Proussevitch, 1998) enables direct comparison of vesicle size distributions with log-based (φ) granulometric measurements. Lognormal (½φ) size bins yield comparable 3D distributions to geometric or linear size bins (sensitivity study presented in Appendix 2, supplementary information), with the advantage that comparisons between vesicle size distributions and grain size/componentry/density distributions are not biased by differences in how the data are binned. The minimum area cut-off for vesicle measurements was set to 5 μm^2 (EqD = 2.5 µm). The number of vesicles in each lognormal size class was normalised by the vesicle- and crystal-free melt area to give 2D number densities, N_a (mm^{-2}). The equivalent 3D number densities, N_v (mm^{-3}) and vesicle volume distributions (VVDs) were calculated using stereological methods (following Mangan et al., 1993; Klug et al., 2002; see

Appendix 2 for detailed methods). Total bubble number densities (BNDs, in mm^3) were calculated by summing N_v values across all size classes >8 μm (following Murtagh and White, 2013), for comparison with other studies.

4. Deposit characteristics and stratigraphy

4.1 Hydromagmatic deposits

Hverfjall edifice

A vertical cross-section through 87.5 m of the edifice stratigraphy is exposed on the interior of the western flank of the tuff ring (site 5.11; Fig. 2c) and is illustrated in Figure S4 (supplementary material). The deposits comprise moderately indurated lapilli-rich beds with a partially palagonised fine ash matrix, and are highly heterogeneous in grain size and sorting throughout the section (Fig. S4c–g). Individual beds are often laterally discontinuous (Fig. S4e); cross-bedding structures are occasionally visible, most commonly in the well-sorted fine-grained ash beds. Lapilli include abundant cored accretionary pellets or coated grains, which comprise dense lithic or scoria fragments surrounded by a fine ash coating (Fig. S4d).

Dense lithic blocks and juvenile bombs up to several tens of centimetres diameter occur throughout the exposed sequence and are accompanied by sediment deformation structures. Large (≤ 1 m) angular blocks of dense basaltic basement are ubiquitous within the crater area (Fig 6b) and define a proximal ballistic field outside of the crater; blocks of ~0.5 m in diameter are found at radial distances of ≤ ~1.5 km from the crater centre (Figs. 2b, S3a). The wide range of lithic diameters observed at all distances from the vent up to ~1.5 km suggests that blocks were ejected at a range of velocities and ejection angles. Ballistic modelling using Eject! software (Mastin, 2001; input parameters summarised in Table S3) yields an initial ejection velocity of ~160 ms^{-1} and ejection angles of 30–45° for a clast of 0.5 m diameter and a density of 2500 kg m^{-3} to reach 1.5 km (Fig. S5). Ejection angles outside this range either require much

higher initial velocities (~200 ms^{-1}) or trajectories that are too shallow for the clast to surmount the existing crater rim. Notably, a minimum initial velocity of 100 ms^{-1} is required to eject a block of any size beyond the current crater rim.

Medial to distal deposits

The opening phase of hydromagmatic activity produced a fine-grained black fall deposit that can be traced to ≤ 20 km and 1 cm thickness (Saemundsson, 1991; Mattsson and Höskuldsson, 2011). This basal pyroclastic fall unit is generally massive, although the base is finer-grained at thicker (20–30 cm) proximal localities (e.g., sites 6.3 and 9.3).

The overall stratigraphic trends are illustrated in Figure 5. The initial fall deposit is overlain by base surge deposits emplaced asymmetrically to the N-NE of the Hverfjall vent (Fig. 3b–f). A maximum deposit thickness of ~7 m was recorded at site 4.7, 1.8 km NE of the vent. Surge deposits thicken into topographic depressions, form pinch and swell structures with significant lateral thickness variations over small distances, and erode to produce characteristic circular landforms (Fig. 3c). Basal surge units are very poorly sorted massive lapilli-tuff, with abundant dense angular lapilli and occasional blocks and bombs within an ash-rich matrix (Fig. 3f, 7). Juvenile bombs of ~5–40 cm deform the underlying bedding, reflecting ballistic emplacement into wet cohesive sediment (Fig. 3g). Tree molds produced by plastering of wet cohesive sediment against tree trunks are inclined directly away from the Hverfjall vent (Einarsson, 1953; Thorarinsson, 1962; Fig. 3h). Where the lower contact is exposed, this basal unit is often underlain by a thin (≤ 1 cm) exposure of the fine-grained black fall deposit, which lies directly above the white silicic Hekla-3 marker bed. The basal massive lapilli-tuff unit is not observed at distances greater than 3.3 km from the Hverfjall vent, even where the basal surge contact is exposed. Sedimentary flow structures include low-angle cross-bedding, antidunes and flute casts (Fig. 3d, i), and indicate highly variable flow conditions. Lapilli are

often concentrated in discontinuous lenses. The sedimentological character of base surge deposits varies laterally.

Above the wet basal surge are clast-supported beds of ash-coated lapilli and coarse ash intercalated with thinly laminated beds of fine to moderately coarse ash (Fig. 5). These stratified lapilli-tuffs are found to distances of 5.5 km, the distal exposure limit of the surge units. The uppermost units are dominated by accretionary lapilli-tuff, with well-sorted clast-supported layers of either lapilli- or coarse ash-sized aggregates (spherical coated particles and AP1 and AP2 accretionary pellets, following the terminology of Brown et al., 2012) separated by thinly laminated fine ash horizons (Figs. 3e, 5). Beds thin upwards to minimum thicknesses of ~1 cm and ~1 mm for the lapilli-rich and lapilli-poor layers, respectively. Thinly bedded ash-rich intervals become dominant (relative to lapilli-rich beds) and are progressively less consolidated with increasing transport distance.

The total bulk volume of hydromagmatic deposits (both fall and surge units) is 0.15 ± 0.02 km^3, of which the basal fall unit comprises 0.08 ± 0.01 km^3. The combined volume of the deposits and the Hverfjall edifice gives a total erupted volume of 0.27 ± 0.03 km^3, at the high end of the range of 10^{-4} to 10^{-1} km^3 (10^5–10^9 m^3) characteristic of tuff cone/tuff ring-forming eruptions (White and Ross, 2011).

4.2 Magmatic deposits

The Jarðbaðshólar scoria cone complex is situated directly north of the Hverfjall tuff ring along the same fissure (Fig. 2), and comprises multiple nested cones of different ages. Eruptive activity at Jarðbaðshólar during the Hverfjall Fires appears to have been concentrated at a single vent, which produced lapilli-dominated scoria fall deposits and lava flows. Scoria lapilli units have a limited dispersal distance (1.3 km), with most of the deposit mass restricted to the cone edifice itself.

The cone edifice comprises outwardly dipping units of scoria lapilli fall (Fig. S6a, supplementary information). Cone-forming deposits are generally massive, with alternating units of thick scoria lapilli and thinner horizons of welded spatter (Fig. S6b). Generally, the base of each scoria lapilli unit comprises relatively fine, well-sorted lapilli; pyroclasts are typically highly vesicular with irregular, angular morphologies bounded by both fluidal and brittly-fractured exterior surfaces. Units are inversely graded over 2 to 4 m, with upper sections comprising both coarse angular lapilli (often with fluidal surfaces) and fluidal bombs flattened parallel to bedding. Bombs are typically < 30 cm along their longest axis, but can reach ~70 cm. The upper contact between each spatter horizon and the overlying fine scoria lapilli unit is generally abrupt.

A massive, clast-supported pyroclastic fall deposit composed of fine scoriaceous lapilli extends to 1.3 km north of the Jarðbaðshólar vent, almost twice the 0.7 km maximum extent previously suggested (Mattsson and Höskuldsson, 2011). This fall unit thins rapidly from > 5 m at 0.2 km (site Q3) to 2.5 cm at 1.3 km (site 9.3). The cone active during the Hverfjall Fires is breached on both eastern and western flanks, and the lava flows can be traced to these breaches. Lava flows travelled towards the east, except a single flow to the west. The contact between lava flow units and magmatic fall deposits is exposed in a fault 0.5 km E–SE of the Jarðbaðshólar cone, where a single lava flow unit (up to 2.5 m thick at site 3.8) stratigraphically overlies the magmatic fall deposit (Fig. S6c, d). Here, the base of the lava flow is in contact with the underlying scoria lapilli deposit, the top of which is welded and flattened by the heat of the overlying flow. The temporal evolution from explosive to effusive activity at Jarðbaðshólar is similar to the behaviour documented at other monogenetic scoria cones (e.g., Heimaey, Iceland; Self et al., 1974; Lathrop Wells, S. Nevada; Valentine et al., 2007) and likely reflects waning mass flux.

4.3 Stratigraphic relationships between magmatic and hydromagmatic deposits

The four deposit types – hydromagmatic fall, hydromagmatic surges, magmatic fall and lava flows – are rarely observed together because of the limited spatial extent of the magmatic units. Nevertheless, several exposed sections show magmatic scoria and/or lava flow units either intercalated within hydromagmatic surge units or directly overlying the basal hydromagmatic fall deposit (Figs. 5, S6d). Unusually, however, an exposure 0.5 km south of the Jarðbaðshólar vent (site 4.1; Fig. 2c) shows vesicular scoria lapilli at the basal contact between the underlying Hekla-3 deposit and the lowermost thin hydromagmatic fall unit from the Hverfjall vent. Coarse lapilli, up to several centimetres in size, were also observed throughout the overlying 60 cm surge sequence, distributed both within and between individual surge beds, suggesting on-going contemporaneous deposition.

Stratigraphic relationships support previous interpretations that magmatic and hydromagmatic vents were active contemporaneously (Mattsson and Höskuldsson, 2011). Although sections at medial sites (6.3 and 9.3) suggest that the deposition of hydromagmatic material (both pyroclastic fall and base surges) began prior to the onset of magmatic fall (Fig. 5), the presence of coarse scoria lapilli directly above Hekla-3 in more proximal sections (4.1) indicates that magmatic and hydromagmatic vents may instead have initiated near-synchronously. However, the early phase of activity at Jarðbaðshólar was probably restricted to proximal cone-building, and therefore did not contribute to the wider tephra blanket. The observed stratigraphic relationships between lava flow units and magmatic fall (both proximal cone-forming and medial deposits) suggest that lava flow emplacement occurred late in the eruptive history of the Jarðbaðshólar vent, after the main phase of cone construction. The presence of finely-stratified surge deposits overlying magmatic fall and lava flow units, even in proximal locations, indicates that explosive activity continued at the Hverfjall vent after

activity ceased at Jarðbaðshólar, thereby demonstrating the longevity of the hydromagmatic activity.

5. Ash characterisation

5.1 Granulometry

Grain size distributions (GSDs) differ markedly between hydromagmatic (Hverfjall tuff ring) and magmatic (Jarðbaðshólar) deposits, with hydromagmatic deposits consistently finer-grained (Fig. 6; Table S4). Ash-sized material (> –1φ or < 2 mm) comprises >89% of the total mass of hydromagmatic samples (basal fall unit), with up to 55% fine ash (> 4φ or < 63 μm) for the most distal samples. The total grain size distribution (TGSD) for the basal fall deposit comprises 97% ash-sized material, with 20% fine ash (dark blue line on Fig. 6b). With increasing distance from the Hverfjall vent, the median grain size of hydromagmatic fall deposits decreases from 1.1φ to 4.2φ (accompanied by an increase in sorting; Fig. S7, supplementary information). In contrast, the median grain sizes of magmatic fall deposit samples are between –4.7φ and –5.8φ with ash-sized material comprising < 12% of the mass. Where hydromagmatic fall and magmatic scoria are observed together, GSDs are bimodal (dashed green curves; Fig. 6a), suggesting contemporaneous deposition and mixing.

5.2 Sample descriptions and componentry

Ash particles from both hydromagmatic and magmatic deposits are almost entirely glassy (sideromelane), with minor phenocrysts of plagioclase, olivine, and clinopyroxene (Fig. 7). Phenocrysts occur as individual crystals, but are more common within crystal aggregates or intergrowths. Many crystals, particularly olivine, exhibit moderately to highly skeletal morphologies indicative of rapid growth (Fig. 7a, b). Incorporation of recycled clasts into large ash particles and lapilli is relatively common, with recycled clasts distinguished by their

475 microcrystalline texture that contrasts with the host sideromelane grain (Fig. 7c). The
476 boundaries between recycled clasts and the host matrix are sharp, and often delineated either
477 by oxide rims (Fig. 7e) or a thin rim of void space (Fig. 7d).

478 Particles were categorised into six component classes based on criteria related to the
479 particle outline, bubble texture, crystal texture, juvenile/non-juvenile character: (1) dense
480 fragments, (2) vesicular particles, (3) shards, (4) microcrystalline grains, (5) free crystals and
481 (6) holocrystalline lithic grains (Table S5, supplementary information). *Dense fragments* are
482 poorly vesicular (0-20% internal vesicles by area) and angular with planar surfaces, and
483 comprise both thin plates and, more commonly, equant blocky grains. Exterior surfaces
484 commonly display stepped fracture patterns with characteristic distributary branching ('river-
485 lines') that indicate brittle fracturing under mixed-mode stresses (Hull, 1999). *Shards* are
486 characterized by highly concave outlines with smooth surfaces from large bounding vesicles.
487 Internal vesicles are few or absent. *Vesicular particles* have internal vesicles that comprise
488 ≥20% to ~75% by area. Apparent 2D bubble-wall thicknesses range from ~50 μm to just a few
489 microns for the most vesicular clasts. Vesicles are mostly round in cross-section, but may be
490 strongly deformed in larger particles (coarse ash and lapilli; Fig. 7c, f). Particle outlines are
491 typically angular, with scalloped edges formed by bounding vesicles with diameters much
492 smaller than the particle, although a small proportion of coarse ash grains show either partial
493 or complete fluidal outer surfaces (Fig. 7g, h). *Microcrystalline grains* contain small
494 plagioclase microlites within a glassy matrix, and are poorly to moderately vesicular. Where
495 present, vesicles are irregular in shape and often deformed around crystals. *Free crystal*
496 particles include both crystal fragments and intact crystals, which are often coated with a thin
497 rim of dense glass. *Lithics* represent the non-juvenile component derived from erosion of the
498 conduit walls or surrounding country rock, and are typically holocrystalline.

The full range of ash components is present in both hydromagmatic and magmatic ash particles over the measured grain size range (0–6φ). Importantly, however, the relative proportions of each component (by number) varies by up to an order of magnitude between different grain-size fractions (Table S5; Fig. 8). In fact, variation in the proportion of different ash components with grain size is much greater than with distance from the vent. For example, in the hydromagmatic fallout ash examined, the proportion of dense fragments increases approximately linearly from 2–3% (at 0φ) to 61–76% (at 5 and 6φ). In contrast, vesicular particles decrease in abundance from 80–88% (at 0φ) to 1–3% (at 5 and 6φ). Component proportions remain relatively constant for the 5φ and 6φ size fractions (i.e., fine ash < 63 μm). The proportion of shards, in contrast, reaches a maximum abundance of 28–36% in the 3φ size fraction. Together, free crystals and lithic grains are minor components of hydromagmatic ash (< 10% of each sample size fraction) except in the in the most proximal sample site 2.3, particularly within the 2φ and 3φ grain size fractions. The proportion of microcrystalline grains is < 6% of all samples, and is almost negligible in the finest size fractions > 2φ. In magmatic ash samples, vesicular particles comprise almost 100% of the 0φ size fraction, but decrease in abundance to 12–13% at 4φ. The relative proportion of dense fragments also increases approximately linearly from 0–1% (at 0φ) to 21–26% (at 4φ), although the absolute proportions of dense fragments are ~20–30% less than in hydromagmatic samples at equivalent size fractions. Magmatic samples lack sufficient material finer than 4φ (< 63 μm) for meaningful componentry measurements of the fine ash fraction.

5.3 Densities

Mean particle densities increase with decreasing grain size (Fig. 9). Hydromagmatic samples also show spatial variations in density. Unusually, the most proximal sample (site 2.3; purple line in Fig. 9) has the lowest-density particles across all size fractions, particularly for grain

sizes < 1φ. Densities of ash grains in this sample range from 1390 (–2φ) to 2630 (4φ) kg m^{-3}, with a mean density of 2150 kg m^{-3}. More generally, ash particles reach a maximum density of 2600–2800 kg m^{-3} for grain sizes >3φ (sites 2.3 and 9.3) or >1φ (site 7.5). The size-density relationship of particles in the proximal magmatic sample, site Q1 (red line in Fig. 9), mirrors that of the hydromagmatic deposit to grain sizes of 4 mm, above which the mean particle density decreases substantially to 600 kg m^{-3}.

The average particle density is coupled to the abundance of vesicular particles in each size fraction: as the proportion of vesicular particles decreases almost linearly from 75–100% at 0φ to 2–10% for size fractions > 3φ, density increases concurrently (Figs. 8, 9). Densities remain constant at a maximum value of ~2700 kg m^{-3} for size fractions > 3φ, which also corresponds to the grain size below which the abundance of vesicular particles becomes negligible.

5.4 Bubble microtextures

Vesicles in all samples are mostly circular in cross-section (Fig. S8; supplementary information), with minor exceptions where vesicles are elongated and deformed around phenocrysts (e.g., Fig. 7f). Importantly, clast vesicularities overlap in hydromagmatic (25% to 75%) and magmatic (53% to 74%) clasts (Table S6; Fig. 1). Bubble number densities (BNDs) are also comparable for hydromagmatic (1.5×10^{12} to 2.5×10^{13} m^{-3}) and magmatic (7.3×10^{12} to 1.4×10^{13} m^{-3}) ash particles, and overlap over a relatively narrow range (Fig. 1). Although low vesicularity clasts extend the range of hydromagmatic BNDs to lower values, BNDs stabilise at $1.45 \pm 0.5 \times 10^{13}$ m^{-3} and are largely independent of vesicularity when > 40% (Fig. 1). Vesicle textures in the quenched rim of a magmatic lapillus (16-32 mm) also lie within the range measured for ash-sized grains. The smaller bubble size in the rim contrasts with the larger bubbles in the expanded lapillus core.

549 Vesicle volume distributions (VVDs) in hydromagmatic clasts are unimodal (except for
550 clasts 9 and 10, which have a second mode resulting from a single large bubble) and are
551 relatively symmetrical about the mode (Fig. 10). Modal volumetric vesicle sizes are positively
552 correlated with vesicularity: low vesicularity clasts (<50%) generally have a common mode in
553 the 45–63 μm size class, moderately vesicular clasts (50–66%) have a broad mode between 45
554 and 125 μm with a peak in the 91–125 μm size class, and high vesicularity clasts (>70%) have
555 slightly positively-skewed distributions with consistently larger modal vesicle sizes in the 125–
556 180 μm size class (Fig. 10). In magmatic clasts, VVDs also vary from the low vesicularity
557 (35%) quenched lapillus rim, which has a broad mode between 45 and 125 μm, to high
558 vesicularity clasts (>55%) where distributions are positively-skewed with a clear mode in either
559 the 125–180 μm or 180–250 μm size classes.
560 The calculated VVDs show that our choice of clast size has not truncated the apparent
561 vesicle size distribution. The maximum vesicle diameter in all clasts is < 500 μm (and most are
562 < 250 μm), which is considerably smaller than the radii of the particles analysed. Furthermore,
563 the size range of vesicles preserved in 1–2 mm ash particles is identical to that in the quenched
564 rim of a 16–32 mm lapillus (Table S6).
565
566 **6. Discussion**
567 The contrasting grain size distributions (GSDs) for hydromagmatic (fall only) and magmatic
568 deposits of the Hverfjall Fires (Fig. 6a) is a recurrent feature of products of wet vs. dry mafic
569 volcanism (Walker and Croasdale, 1971; Walker 1971; Houghton and Nairn, 1991; Liu et al.,
570 2015). The greater ash content of hydromagmatic samples reflects elevated fragmentation
571 efficiencies; however the ash content at a given distance from the vent may be substantially
572 augmented by moisture-induced deposition by aggregation and *en masse* sedimentation.
573 Therefore, to be meaningful, total grain size distributions (TGSDs) of deposits should be

574 compared, rather than GSDs from individual locations. The TGSD calculated for the Hverfjall
575 hydromagmatic fall deposit lies within the global range of proximal mafic hydromagmatic
576 GSDs (Fig. 6b; compiled by Liu et al., 2015a), and is in good agreement with measurements
577 of the Eggoya eruption of Jan Mayan, which represents the only other estimated TGSD for a
578 tuff cone/tuff ring-forming eruption (Gjerlow et al., 2015). We do not have sufficient data to
579 construct a TGSD from the 'dry' magmatic deposit; however, based on exposures to 1.5 km,
580 we are confident that the ash content is much lower than the hydromagmatic fall unit studied.
581 There are very few TGSDs for cinder cone eruptions, but data from Cerro Negro (Rose et al.,
582 1973), Izu-Oshima (Mannen, 2006), Heimaey (Self et al., 1974) and Al-Madinah (Kawabata
583 et al., 2015) suggest that the fine ash content of scoria cone eruptions is negligible, and that
584 most (> 90–95%) of the fragmented material is > 1 mm in size.
585 The TGSD produced by an eruption is controlled by the fragmentation process and the
586 characteristic vesicle size (Rust and Cashman, 2011). Figure 11 compares the size distributions
587 of particles and bubbles for (a) magmatic and (b) hydromagmatic (fall only) deposits from the
588 Hverfjall Fires. Most strikingly, the size ranges of vesicles and particles overlap for
589 hydromagmatic deposits, but are separated by several orders of magnitude in magmatic
590 deposits. This difference between hydromagmatic and magmatic patterns of vesicle and
591 particle size data is consistent with published data from other magmatic (e.g., Rust and
592 Cashman, 2011) and hydromagmatic (e.g., Liu et al., 2015a) eruptions of low-H_2O basalt (see
593 also Fig. 11); it also suggests that fragmentation processes occurring at the Hverfjall and
594 Jarðbaðshólar vents were mechanically distinct. In the following discussion, we integrate
595 observations from a diverse suite of pyroclast measurements to compare and contrast the
596 eruptive processes operating at magmatic and hydromagmatic vents during the Hverfjall Fires.
597
598 **6.1 How do particle sizes, shapes and textures co-vary?**

599 The physical properties of erupted pyroclasts record the magmatic conditions prior to and
600 during fragmentation; if unmodified by post-fragmentation processes, particle shape preserves
601 information about the fragmentation regime (i.e., brittle vs. ductile; Büttner et al., 2002; Liu et
602 al., 2015b), whilst internal vesicle (and crystal) textures preserve information on the conditions
603 of magma ascent (e.g., Klug and Cashman, 1994; Cashman and Blundy, 2000; Cashman et al.,
604 2004; Lautze and Houghton, 2007; Wright et al., 2012; Rust and Cashman, 2011; Stovall et al.,
605 2011; Stovall et al., 2012; Alfano et al., 2011; Murtagh and White, 2013; Cioni et al., 2014).
606 Differences in the size, shape, and number density of bubbles that intersect particle surfaces
607 can account for much of the morphological diversity within ash samples such that, for a given
608 bubble population, particle shape and texture vary predictably between different grain-size
609 classes (Genareau et al., 2012; Rausch et al., 2015; Liu et al., 2015a,b).

610 Our componentry data show that the ash components – dense fragments, vesicular particles
611 and shards – are the same in both the magmatic and hydromagmatic deposits, and have
612 proportions that vary systematically as a function of grain size (Fig. 8). Density data (Fig. 9)
613 further illustrate the increasing importance of internal vesicles at grain sizes < 0φ (> 1 mm). At
614 this grain size, the particle size exceeds the maximum bubble size and the relative length-scales
615 of bubbles and particles are sufficiently distinct that all particles can be classed as vesicular,
616 and the individual particle morphology is independent of the bubble size distribution.

617 The size distributions of bubbles and particles progressively overlap and interact at particle
618 sizes >0φ (<1 mm). As the length-scale of fragmentation approaches the modal bubble size,
619 the size of bubbles increases relative to that of particles. This is reflected by an approximately
620 linear increase in the proportions of both dense fragments and shards as the particle size
621 decreases from 0φ to 4φ. Dense fragments form by brittle fracture at a length-scale smaller
622 than the local size distribution of bubbles. They are most abundant in the 4φ size fraction,
623 which corresponds to the modal vesicle sizes in clasts of low to moderate vesicularity (< 60%;

Fig. 10). Shards represent the interstices between closely spaced bubbles and are most common in the 3φ size fraction, which corresponds to the modal vesicle sizes in high vesicularity clasts (> 60%; Fig. 10).

The componentry data can be combined with the grain size data to produce total component distributions (TCDs; Fig. 12). Here the distinction between magmatic and hydromagmatic deposits becomes clear. Magmatic deposits are dominated by particle sizes > 1 mm, and therefore comprise, overwhelmingly, vesicular grains. In contrast, 90% of the total mass of the hydromagmatic deposit is > 0φ, with a broad mode in the TGSD between 1 and 4φ (63–500 μm), and the component assemblage is dominated by dense fragments. Interestingly, however, although dense fragments dominate the hydromagmatic deposit by number (Fig. 12a), the TCD shows that by mass they actually contribute a smaller proportion than vesicular particles (Fig. 12b).

To summarise, size-dependent variations in the proportions of different ash components are independently supported by corresponding measurements of mean particle density and vesicle texture, and are attributed to a bubble control on the scale and geometry of brittle fracture. That this is a general phenomenon is illustrated by comparing hydromagmatic ash from Hverfjall with ash deposits from the opening hydromagmatic phase of the 2011 Grímsvötn eruption (Fig. 13). There is a striking agreement between the relative proportions of dense to 'bubbly' (vesicular particles and shards) grains in hydromagmatic Hverfjall and Grímsvötn deposits over the shared range of grain sizes, which suggests that both the size and spatial distributions of bubbles in magma at the point of fragmentation were similar in the two eruptions.

6.2 Vesiculation during the Hverfjall Fires

A key observation from our study is that the vesicle textures, as measured by bubble number densities (BNDs), are similar for hydromagmatic and magmatic clasts from the Hverfjall Fires deposits (Fig. 1). As these pyroclasts have similar glass compositions (Liu, 2016), BNDs can be considered a proxy for relative magma decompression rate (Cashman and Mangan, 1994; Hurwitz and Navon, 1994; Toramaru et al., 2006; Mangan et al., 2004; Rust and Cashman, 2011; Lautze and Houghton, 2005; Murtagh and White, 2013; Mangan et al., 2014). By this reasoning, the overlapping BNDs suggest similar magma ascent rates for both the magmatic and hydromagmatic vents. Using the empirical relation from Mangan et al. (2014), the observed BNDs correspond to mass eruption rates of 10^5 to 10^7 kg s^{-1} (hydromagmatic) and 10^6 to 10^7 kg s^{-1} (magmatic), both with an average of ~1.2×10^7 kg s^{-1}. The range of mass eruption rates for both magmatic and hydromagmatic vents overlap those typical of mafic lava fountain eruptions (10^5 to 10^6 kg s^{-1}; Mangan et al., 2014), but extend an order of magnitude higher.

The vesicularities of Hverfjall Fires clasts are broadly similar to those measured in clasts from other mafic eruptions of low-H_2O and low crystallinity magmas (Fig. 1). Most important is the wide range in the vesicularity of hydromagmatic clasts relative to those of magmatic eruptions. The broad vesicularity distributions of hydromagmatic deposits are generally attributed to either the spatial heterogeneity of an immature bubble population, or to fragmentation and quenching at different stages of vesiculation (e.g. Houghton and Wilson, 1989; Murtagh and White, 2013; Mastin et al., 2004). Figure 1 shows, however that the vesicularities of both magmatic and hydromagmatic clasts from the Hverfjall Fires overlap between ~50% and 75%, supporting the growing recognition that vesicularity is not a robust criterion to distinguish the eruptive products of magmatic from hydromagmatic fragmentation (Murtagh and White, 2013; Graettinger et al., 2013; White and Valentine, 2016).

Bubble number densities (BNDs) are also similar in the magmatic and hydromagmatic clasts from the Hverfjall Fires, although BNDs of hydromagmatic clasts are, on average, slightly higher. Figure 1 shows that BND data from the literature is more variable than the Hverfjall Fires in both magmatic and hydromagmatic samples. Much of the textural range in magmatic samples is interpreted to result from post-fragmentation processes. Our data support this interpretation, as BNDs of hydromagmatic Hverfjall clasts and rims of magmatic clasts are similar to those of rapidly quenched rims of Kilauea Iki lapilli (Stovall et al., 2011; Porritt et al., 2012).

Textural similarities between magmatic and hydromagmatic bubble populations indicate that differences in the vesiculation history cannot explain the contrasting fragmentation efficiencies. In the following section, we combine field observations with pyroclast measurements to discuss the controls on both fragmentation and eruptive style. In particular, we consider the contribution of differential cooling rates, and the resulting thermal stresses, to fine fragmentation of hydromagmatic pyroclasts.

6.3 Eruptive processes during the Hverfjall Fires

6.3.1 Jarðbaðshólar scoria cones

Magmatic activity at Jarðbaðshólar produced a coarse deposit dominated by scoriaceous lapilli and bombs, where pyroclast grain sizes are decoupled in scale from vesicle sizes by almost two orders of magnitude (Fig. 11). The grain size and morphological/textural properties of magmatic pyroclasts are comparable to those of other crystal-poor basaltic eruptions that involved no MWI (e.g., Kilauea, Hawaii; Parfitt, 1998; Mangan and Cashman, 1996) and are consistent with a fragmentation regime dominated by fluidal (inertial) break-up of low-viscosity magma. Under this regime, rapid bubble nucleation and expansion accelerates the melt phase, but does not directly contribute to the fragmentation process (Rust and Cashman,

2011). Compared to erupted lava volumes, ash production was negligible and tephra deposition was largely confined to proximal vent regions (Einarsson et al., 1991; Mattsson and Höskuldsson, 2011).

6.3.2 Hverfjall tuff ring

Hydromagmatic activity at the Hverfjall vent produced fine-grained unconsolidated ash fall, and poorly-sorted indurated base surges, deposits rich in ash and accretionary-lapilli. The transition from fall- to surge-dominated deposition has previously been attributed to a reduction in volumetric magma flux, and hence a reduced ratio of magma to water in the vent, coincident with the onset of activity at Jarðbaðshólar (Mattsson and Höskuldsson, 2011). Lowering of the magma-water ratio is widely associated with a decrease in the efficiency of MWI (e.g., Heiken and Wohletz, 1985; Wohletz, 1986). It is important to note, however, that the bulk volumetric proportions of magma and water in an environment of interaction do not necessarily translate to the proportions involved in direct interaction (White and Valentine, 2016). Furthermore, the presence of surge deposits prior to the main phase of magmatic tephra fall from Jarðbaðshólar (Figs. 5, S6) suggests that an additional mechanism is required to account for the change in interaction efficiency, such as a build-up of clastic material within the vent.

Our textural and componentry data demonstrate that the Hverfjall Fires magma was already vesiculating when it encountered groundwater and that the external water supply was sufficient to maintain MWI throughout the eruption, with no evidence for progressive exhaustion of a finite water reservoir. We propose that the spatial distribution of MWI (both laterally and stratigraphically) was determined by the pre-existing regional hydrology (Fig. 2a), where a propagating dike interacted with aquifers hosted within permeable basalt lavas. The large dimensions of the Hverfjall edifice relative to ‘average’ tuff rings, particularly the height of the crater rim (White and Ross, 2011), may also reflect this prolonged activity. The high

722 permeability, and thus the discharge rate of lava flow-hosted aquifers, are consistent with the
723 continuous water supply required to maintain MWI, as observed for similarly 'over-sized' tuff
724 rings/cones in coastal littoral settings such as in Hawaii and the Galapagos (Lorenz, 1986,
725 2003).

726 Invoking a groundwater source raises the question of why hydromagmatic (or more
727 specifically, phreatomagmatic) activity was confined to the Hverfjall vent whilst Jarðbaðshólar
728 remained 'dry', especially as the two coeval vents are < 5 km apart and within a few metres in
729 elevation (Fig. 2). One possibility is that conductive heat flow from the laterally-propagating
730 dike feeding the Hverfjall vent locally dried up the groundwater in the area surrounding
731 Jarðbaðshólar (Mattsson and Höskuldsson, 2011). Our data can neither prove nor disprove this
732 hypothesis. We note, however, the Hverfjall tuff ring is situated almost directly above the
733 modern confluence of the two major groundwater flows (Einarsson, 2004), and therefore at
734 local maxima in groundwater flow rate (Fig. 2). Jarðbaðshólar, in contrast, appears to lie above
735 a 'shadow' where the groundwater is deflected to the south, perhaps due to reduced
736 permeability through the highly altered (palagonised) Námafjall hyaloclastite ridge directly to
737 the east of Jarðbaðshólar (DePaolo et al., 2001; Jarosch et al., 2008). In this scenario, the spatial
738 distribution of phreatomagmatic activity is directly controlled by the pre-existing regional
739 hydrological regime. A similar environmental control has been proposed to account for the
740 distribution of phreatomagmatic vents within the Auckland Volcanic Field, New Zealand
741 (Nemeth et al., 2012).

742

743 **6.3.3 The influence of cooling rate on hydromagmatic fragmentation**

744 The angular morphology of ash grains, together with the ubiquity of 'river-line' fracture
745 patterns (Hull, 1999) on exterior surfaces, indicates that brittle fragmentation dominates the
746 formation of ash-sized pyroclasts. Brittle fragmentation requires that the timescale of

747 deformation be shorter than the structural relaxation timescale (i.e., the melt crosses the glass
748 transition; Dingwell and Webb, 1989). At typical magmatic temperatures, brittle fragmentation
749 of low viscosity basaltic melts requires exceptionally high strain rates. The conditions for brittle
750 fragmentation during MWI, in contrast, are easily established by rapid cooling of magma
751 during interaction with external water (Mastin et al., 2004; Liu et al., 2015a; Van Otterloo et
752 al., 2015). Interestingly, the presence of either complete or partial fluidal exterior surfaces on
753 some particles (Fig. 7g,h) suggests prior (or contemporaneous) hydrodynamic break-up. Rapid
754 magma ascent, as suggested by high BNDs, may have contributed to the development of
755 hydrodynamic instabilities (Mangan and Cashman, 1996).

756 Magma cooling rates during MWI are sufficient to generate the high thermal stresses
757 required to exceed the thermal stress resistance (TSR) of silicate glass (Schmidt et al. 2010;
758 Schipper et al., 2011; Van Otterloo, 2015). Depending on the magnitude of thermal stress (a
759 function of cooling rate and particle size, as well as material properties such as glass
760 composition or bulk porosity), brittle failure can occur either during or after solidification (e.g.,
761 Chandrasekar and Chaudhri, 1994; Patel et al., 2013). In this way, thermal stresses may trigger
762 synchronous, or secondary, brittle fragmentation of pyroclasts formed hydrodynamically
763 during volatile-driven acceleration (Schmidt et al. 2010; Schipper et al., 2011; Liu et al., 2015a;
764 Jutzeler et al., 2016). In contrast to the process of 'turbulent shedding' (Mastin et al., 2004;
765 Mastin et al., 2007), during which brittle fragmentation is limited to the shedding of glassy
766 rinds formed on larger particles under turbulent cooling conditions, we propose that thermal
767 stress can cause wholesale disintegration of pyroclasts.

768 If MWI occurs at sufficiently low pressure for volatile saturation then the magma will
769 contain gas bubbles, as was clearly the case for the Hverfjall Fires eruption. The presence of
770 bubbles (voids) reduces the overall strength, thus rendering the magma more susceptible to
771 breakage under any applied stress (e.g., Heap et al., 2014; Van Otterloo et al., 2015). In the

772 context of quench granulation, this strength weakening reduces the maximum TSR, enabling
773 fracturing at lower tensile thermal stresses (Zimanowski et al., 2003). Bubbles in glass can also
774 influence the propagation and acceleration of brittle fractures by focusing fracture paths
775 towards stress concentrations around bubbles (Green et al., 1977; Broek et al., 2012; Van
776 Otterloo et al., 2015).

777 The efficiency of (pyroclast-producing) fragmentation was likely enhanced by the rapid
778 thermal expansion of external water/steam during confined mixing, such as occurs during
779 littoral explosions (Jurado-Chichay et al. 1996; Mattox and Mangan 1997) and which could
780 also take place within an in-vent water-saturated slurry of fragmented lithic and pyroclastic
781 material. Mixing/mingling between magma and an in-vent water-saturated sediment slurry was
782 first proposed by Kokelaar (1986) and subsequently expanded in light of textural observations
783 and thermodynamic considerations of ubiquitous entrained clasts in composite scoria lapilli
784 and bombs from Surtseyan eruptions (White et al., 1996; Schipper and White, 2016). The
785 abundance of lithic blocks and lapilli of dense basalt both in and around the Hverfjall tuff ring
786 crater (Fig. 3h, S3a, supplementary information) provides evidence of disruption of the
787 basement substrate by subsurface explosions. Although the homogeneous lithology of
788 basement rocks means that the lithic assemblage provides little indication of the absolute depth
789 of disruption, the presence of lithic material throughout the depositional sequence requires
790 either continuous country rock excavation (e.g., Lorenz, 1986, 2003) or recycling and ejection
791 of earlier disrupted material (Graettinger et al., 2014; Valentine et al., 2015). The development
792 of an in-vent slurry would support the latter hypothesis (Kokelaar, 1986; Schipper and White,
793 2016), without the need to invoke continuous vent widening or vertical excavation to account
794 for the erupted lithic assemblage. Together, the incorporation of recycled clasts within coarse
795 ash and lapilli from the Hverfjall vent (Fig. 7c-e), the abundance of fine ash within outer and

internal (in 2D) vesicles, and the presence of thick ash-rich rinds on accretionary lapilli throughout the exposed crater section (Fig. S4), all lend further support to the slurry hypothesis.

The styles of magmatic (volatile-driven inertial break-up) and hydromagmatic (steam explosivity and/or thermal brittle disintegration) fragmentation inferred for Hverfjall are not mutually exclusive; moreover, plausible feedbacks exist whereby one process could trigger or amplify the other (e.g., Wohletz and Sheridan, 1983; Wohletz, 1986; Zimanowski et al., 1991; Zimanowski et al., 1997; Graettinger et al., 2013). For example, initial fluidal fragmentation could provide the inertia to drive fuel-coolant mixing with sufficient surface area to enable MFCI and associated fragmentation. Further brittle fragmentation due to thermal stress in the rapidly-cooled glass may then occur during the subsequent expansion phase. Fragmentation during hydromagmatic eruptions likely occurs via a combination of all three processes, with spatial and/or temporal variation in the relative dominance of each mechanism.

7. Conclusions

The textures of hydromagmatic pyroclasts erupted during the Hverfjall Fires fissure eruption reveal that considerable vesiculation took place prior to magma-water interaction (MWI). Overlapping vesicularity and bubble number density distributions in rapidly quenched pyroclasts from both magmatic and hydromagmatic deposits echo the similarities seen in mafic pyroclasts more generally, and suggest comparable ascent (decompression) paths. Further, co-variation in particle size, shape and texture over the full range of available grain sizes suggest that hydromagmatic fragmentation occurred principally by brittle mechanisms, where the length-scale and geometry of fracturing was controlled by the bubble population at the time of MWI. Interestingly, whilst ash with a ‘blocky’ morphology dominates the hydromagmatic deposit at grain sizes smaller than the modal bubble size, vesicular particles and bubble shards comprise the bulk of the deposit by mass when the total grain size distribution is considered.

Together these data support previous evidence from the 2011 Grímsvötn eruption, Iceland, that the shape and size distributions of hydromagmatic pyroclasts are strongly influenced by the dynamics of vesiculation prior to MWI and fragmentation (Liu et al., 2015a).

Interestingly, the preservation of partial fluidal outer surfaces on some ash-sized pyroclasts suggests that not only was the magma vesiculating when it encountered groundwater, but also that it may have been partially fragmented. As the pressure gradient between non-fragmented ascending magma and an adjacent aquifer under hydrostatic pressure would drive water away from the conduit, we suggest that magmatic fragmentation may be a pre-requisite for efficient magma-water interaction. Whether that interaction takes place at the conduit margins or by magma fountaining into a wet crater would depend on the depth of the groundwater table relative to the fragmentation surface, which may vary throughout an eruption (e.g., Mastin, 1997).

We propose that the elevated fragmentation efficiency of hydromagmatic deposits is driven, at least in part, by residual thermal stresses in glass quenched during MWI (e.g., Dürig et al., 2012; Liu et al., 2015a). We explain fine fragmentation by magmatic vesiculation followed by rapid quenching and brittle breakage, which does not necessarily require pre-mixing of magma and water. Moreover, different mechanisms of magma fragmentation – explosivity by expansion of exsolved magmatic volatiles, steam explosivity, and thermal granulation – are likely to operate simultaneously during hydromagmatic eruptions, with varying dominance in response to fluctuations in the magma supply or the availability of external water. In summary, we view magmatic volatile-driven and hydromagmatic fragmentation as end-members of a spectrum, rather than discrete eruptive states, and urge caution when interpreting MWI based on the properties of fine ash alone.

Acknowledgements

The authors with to thank T. Thordarson and an anonymous reviewer for their careful and constructive reviews that greatly improved this manuscript. This work was completed with support for KVC from the AXA Research Fund and a Royal Society Wolfson Merit Award, a Royal Society URF to ACR, and a University of Bristol postgraduate Scholarship to EJL. Fieldwork was supported by a New Researchers Award from the Geologists' Association to EJL. We thank S. Kearns and B. Buse for their assistance with SEM analysis.

References

Alfano, F., Bonadonna, C., Delmelle, P. & Costantini, L. (2011), Insights on tephra settling velocity from morphological observations, Journal of Volcanology and Geothermal Research 208(3-4), 86–98.

Aranda-Gómez, J. & Luhr, J. F. (1996), Origin of the Joya Honda maar, San Luis Potosi, Mexico, Journal of Volcanology and Geothermal Research 74(1), 1–18.

Bonadonna, C. & Houghton, B. (2005), Total grain-size distribution and volume of tephra-fall deposits, Bulletin of Volcanology 67(5), 441–456.

Bonadonna, C., Biass, S. & Costa, A. (2015), Physical characterization of explosive volcanic eruptions based on tephra deposits: Propagation of uncertainties and sensitivity analysis, Journal of Volcanology and Geothermal Research 296, 80–100.

Broek, D. (2012), Elementary engineering fracture mechanics, Springer Science & Business Media.

Brown, R. J., Bonadonna, C. & Durant, A. J. (2012), A review of volcanic ash aggregation, Physics and Chemistry of the Earth 45-46, 65–78.

Büttner, R., Dellino, P. & Zimanowski, B. (1999), Identifying magma-water interaction from the surface features of ash particles, Nature 401(6754), 688–690.

Büttner, R., Dellino, P., La Volpe, L., Lorenz, V. & Zimanowski, B. (2002), Thermohydraulic explosions in phreatomagmatic eruptions as evidenced by the comparison between pyroclasts and products from Molten Fuel Coolant Interaction experiments, Journal of Geophysical Research - Solid Earth 107(B11), 2277.

875 Cashman, K. (2004), Volatile controls on magma ascent and eruption, in Sparks, RSJ and
876 Hawkesworth, CJ, ed., 'State of the Planet: Frontiers and Challenges in Geophysics', Vol. 150
877 of American Geophysical Monograph, 109–124.

878 Cashman, K. & Blundy, J. (2000), Degassing and crystallization of ascending andesite and
879 dacite, Philosophical Transactions of the Royal Society of London A: Mathematical, Physical
880 and Engineering Sciences 358(1770), 1487–1513.

881 Cashman, K. V. & Mangan, M. T. (1994), Physical aspects of magmatic degassing; II,
882 Constraints on vesiculation processes from textural studies of eruptive products, Reviews in
883 Mineralogy and Geochemistry 30(1), 447–478.

884 Cashman, K. V., Deligne, N. I., Gannett, M. W., Grant, G. E. & Jefferson, A. (2009), Fire and
885 water: Volcanology, geomorphology, and hydrogeology of the Cascade Range, central Oregon,
886 Field Guides 15, 539–582.

887 Chandrasekar, S. & Chaudhri, M. (1994), The explosive disintegration of Prince Ruperts
888 Drops, Philosophical Magazine B - Physics of Condensed Matter Statistical Mechanics
889 Electronic Optical and Magnetic Properties 70(6), 1195–1218.

890 Chough, S. & Sohn, Y. (1990), Depositional mechanics and sequences of base surges,
891 Songaksan tuff ring, Cheju Island, Korea, Sedimentology 37(6), 1115–1135.

892 Cioni, R., Pistolesi, M., Bertagnini, A., Bonadonna, C., Hoskuldsson, A. & Scateni, B. (2014),
893 Insights into the dynamics and evolution of the 2010 Eyjafjallajökull summit eruption (Iceland)
894 provided by volcanic ash textures, Earth and Planetary Science Letters 394, 111–123.

895 Cioni, R., Sbrana, A. & Vecci, R. (1992), Morphologic features of juvenile pyroclasts from
896 magmatic and phreatomagmatic deposits of Vesuvius, Journal of Volcanology and Geothermal
897 Research 51(1), 61–78.

898 Cole, P., Guest, J., Duncan, A. & Pacheco, J.M. (2001), Capelinhos 1957–1958, Faial, Azores:
899 deposits formed by an emergent surtseyan eruption, Bulletin of volcanology 63(2-3), 204–220.

900 Colgate, S. A. & Sigurgeirsson, T. (1973), Dynamic mixing of water and lava, Nature 244, pp.
901 552–555.

902 Daggitt, M.L., Mather, T.A., Pyle, D.M. & Page, S., (2014), AshCalc–a new tool for the
903 comparison of the exponential, power-law and Weibull models of tephra deposition. Journal of
904 Applied Volcanology, 3, 7.

905 Dellino, P., Guðmundsson, M. T., Larsen, G., Mele, D., Stevenson, J. A., Thordarson, T. &
906 Zimanowski, B. (2012), Ash from the Eyjafjallajokull eruption (Iceland): Fragmentation
907 processes and aerodynamic behavior, Journal of Geophysical Research - Solid Earth 117,
908 B00C04.

909 DePaolo, D. J., Stolper, E. & Thomas, D. M. (2001), Deep drilling into a Hawaiian volcano,
910 EOS Transactions 82(13), 149–154.

911 Di Traglia, F., Cimarelli, C., De Rita, D. & Torrente, D. G. (2009), Changing eruptive styles
912 in basaltic explosive volcanism: examples from Croscat complex scoria cone, Garrotxa
913 Volcanic Field (NE Iberian Peninsula), Journal of Volcanology and Geothermal Research
914 180(2), 89–109.

915 Dürig, T. and Zimanowski, B., (2012). “Breaking news” on the formation of volcanic ash:
916 Fracture dynamics in silicate glass. Earth and Planetary Science Letters, 335, 1-8.

917 Einarsson, A. (1982), The palaeolimnology of Lake Mývatn, northern Iceland: plant and
918 animal microfossils in the sediment, Freshwater Biology 12(1), 63–82.

919 Einarsson, Á., Stefánsdóttir, G., Jóhannesson, H., Ólafsson, J. S., Gíslason, G. M., Wakana, I.,
920 Gudbergsson, G. & Gardarsson, A. (2004), The ecology of Lake Mývatn and the River Laxá:
921 variation in space and time, Aquatic Ecology 38(2), 317–348.

922 Einarsson P. (1991) Umbrotin við Kröflu 1975–1989. In: Garðarsson A, Einarsson Á (eds)
923 Náttúra Mývatns. Hið íslenska náttúrufræðifélag, Reykjavík.

924 Engwell, S., Sparks, R. & Aspinall, W. (2013), Quantifying uncertainties in the measurement
925 of tephra fall thickness, Journal of Applied Volcanology 2(1), 1–12.

926 Eychenne, J., Le Pennec, J.-L., Troncoso, L., Gouhier, M. & Nedelec, J.-M. (2012), Causes
927 and consequences of bimodal grain-size distribution of tephra fall deposited during the August
928 2006 Tungurahua eruption (Ecuador), Bulletin of volcanology 74(1), 187–205.

929 Fierstein, J. & Nathenson, M. (1992), Another look at the calculation of fallout tephra volumes,
930 Bulletin of Volcanology 54(2), 156–167.

931 Genareau, K., Proussevitch, A. A., Durant, A. J., Mulukutla, G. & Sahagian, D. L. (2012),
932 Sizing up the bubbles that produce very fine ash during explosive volcanic eruptions,
933 Geophysical Research Letters 39, L15306.

934 Gilbert, J. S. & Lane, S. (1994), The origin of accretionary lapilli, Bulletin of Volcanology
935 56(5), 398–411.

936 Gíslason, S., Eiríksdóttir, E., Galeczka, I., Stefánsdóttir, G., Pfeffer, S., Johannsson, T., Bali,
937 E., Sigmarsson, O., Stefánsson, A., Keller, N. & Sigurdsson, Ã. (2015), Environmental

pressure from the 2014-15 eruption of the Bardarbunga volcano, Iceland, Geochemical Perspectives Letters (2015) 1, 84-93 | doi: 10.7185/84 geochemlet.1509 1, 84–93.

Gjerløw, E., Höskuldsson, A. & Pedersen, R.-B. (2015), The 1732 Surtseyan eruption of Eggøya, Jan Mayen, North Atlantic: deposits, distribution, chemistry and chronology, Bulletin of Volcanology 77(2), 1–21.

Grættinger, A. H., Skilling, I., McGarvie, D. & Höskuldsson, Á. (2013), Subaqueous basaltic magmatic explosions trigger phreatomagmatism: A case study from Askja, Iceland, Journal of Volcanology and Geothermal Research 264, 17–35.

Grættinger, A., Valentine, G., Sonder, I., Ross, P.S., White, J. & Taddeucci, J. (2014), Maar-diatreme geometry and deposits: Subsurface blast experiments with variable explosion depth, Geochemistry, Geophysics, Geosystems 15(3), 740–764.

Green, D., Nicholson, P. S. & Embury, J. (1977), Crack shape studies in brittle porous materials, Journal of Materials Science 12(5), 987–989.

Heap, M. J., Xu, T. & Chen, C.-f. (2014), The influence of porosity and vesicle size on the brittle strength of volcanic rocks and magma, Bulletin of Volcanology 76(9), 1–15.

Heiken, G. & Wohletz, K. (1985), Volcanic ash, University Presses of California, Chicago, Harvard & MIT.

Heiken, G. H. (1971), Tuff rings: Examples from the Fort Rock-Christmas Lake Valley Basin, south-central Oregon, Journal of Geophysical Research 76(23), 5615–5626.

Hjartardóttir, Á. R., Einarsson, P., Bramham, E. & Wright, T. J. (2012), The Krafla fissure swarm, Iceland, and its formation by rifting events, Bulletin of volcanology 74(9), 2139–2153.

959 Houghton, B. & Gonnermann, H. (2008), Basaltic explosive volcanism: constraints from
960 deposits and models, Chemie der Erde-Geochemistry 68(2), 117–140.

961 Houghton, B. & Hackett, W. (1984), Strombolian and phreatomagmatic deposits of Ohakune
962 Craters, Ruapehu, New Zealand: a complex interaction between external water and rising
963 basaltic magma, Journal of volcanology and geothermal research 21(3), 207–231.

964 Houghton, B. & Nairn, I. (1991), The 1976−1982 Strombolian and phreatomagmatic eruptions
965 of White Island, New Zealand: Eruptive and depositional mechanisms at a 'wet' volcano,
966 Bulletin of volcanology 54(1), 25–49.

967 Houghton, B. & Wilson, C. (1989), A vesicularity index for pyroclastic deposits, Bulletin of
968 volcanology 51(6), 451– 462.

969 Houghton, B., Wilson, C. & Smith, I. (1999), Shallow-seated controls on styles of explosive
970 basaltic volcanism: a case study from New Zealand, Journal of Volcanology and Geothermal
971 Research 91(1), 97–120.

972 Hreinsdóttir, S., Sigmundsson, F., Roberts, M. J., Björnsson, H., Grapenthin, R., Arason, P.,
973 Árnadóttir, T., Hólmjárn, J., Geirsson, H., Bennett, R. A. et al. (2014), Volcanic plume height
974 correlated with magma-pressure change at Grimsvotn Volcano, Iceland, Nature Geoscience
975 7(3), 214–218.

976 Hull, D. (1999), Fractography, Cambridge University Press.

977 Hurwitz, S. & Navon, O. (1994), Bubble nucleation in rhyolitic melts: Experiments at high
978 pressure, temperature, and water content, Earth and Planetary Science Letters 122(3), 267–280.

Jarosch, A., Gudmundsson, M. T., Högnadóttir, T. & Axelsson, G. (2008), Progressive cooling of the hyaloclastite ridge at Gjálp, Iceland, 1996–2005, Journal of Volcanology and Geothermal Research 170(3), 218–229.

Jutzeler, M., White, J. D., Proussevitch, A. A. & Gordee, S. M. (2016), Vesiculation and fragmentation history in a submarine scoria cone-forming eruption, an example from Nishiizu (Izu Peninsula, Japan), Bulletin of Volcanology 78(2), 1–25.

Kiernan, K., Wood, C. & Middleton, G. (2003), Aquifer structure and contamination risk in lava flows: insights from Iceland and Australia, Environmental Geology 43(7), 852–865.

Kingery, W. D. (1955), Factors affecting thermal stress resistance of ceramic materials, Journal of the American Ceramic Society 38(1), 3–15.

Kjaran, S. & Hólm, S. (1999), Mývatn. Grunnvatnslíkan af vatnasvidi Mývatns, Technical report, Verkfrædistofan Vatnaskil.

Klug, C. & Cashman, K. (1994), Vesiculation of May 18, 1980, Mount St-Helens magma, Geology 22(5), 468–472. Klug, C., Cashman, K. & Bacon, C. (2002), Structure and physical characteristics of pumice from the climactic eruption of Mount Mazama (Crater Lake), Oregon, Bulletin of Volcanology 64(7), 486–501.

Knutsson, G. (2008), Hydrogeology in the Nordic countries, Episodes 31(1), 148–154.

Kokelaar, P. (1986), Magma-water interactions in subaqueous and emergent basaltic, Bulletin of Volcanology 48(5), 275–289.

Kononov, V. (1979), Hydrogeology of Iceland, International Geology Review 21(4), 385–398.

999 Kristmannsdóttir, H. & Ármannsson, H. (2004), Groundwater in the Lake Mývatn area,
1000 northern Iceland: Chemistry, origin and interaction, Aquatic Ecology 38(2), 115–128.

1001 Kshirsagar, P., Siebe, C., Guilbaud, M. N. & Salinas, S. (2016), Geological and environmental
1002 controls on the change of eruptive style (phreatomagmatic to Strombolian-effusive) of Late
1003 Pleistocene El Caracol tuff cone and its comparison with adjacent volcanoes around the Zacapu
1004 basin (Michoacán, México), Journal of Volcanology and Geothermal Research 318, 114–133.

1005 Lautze, N. C. & Houghton, B. F. (2005), Physical mingling of magma and complex eruption
1006 dynamics in the shallow conduit at Stromboli volcano, Italy, Geology 33(5), 425–428.

1007 Lautze, N. C. & Houghton, B. F. (2007), Linking variable explosion style and magma textures
1008 during 2002 at Stromboli volcano, Italy, Bulletin of Volcanology 69(4), 445–460.

1009 Liu, E.J (2016), The generation of volcanic ash during basaltic hydromagmatic eruptions: From
1010 fragmentation to resuspension. PhD Thesis, University of Bristol.

1011 Liu, E.J, Cashman, K.V & Rust, A.C (2015a), Optimising shape analysis to quantify volcanic
1012 ash morphology, GeoResJ 8, 14–30.

1013 Liu, E.J, Cashman, K.V, Rust, A.C & Gislason, S. (2015b), The role of bubbles in generating
1014 fine ash during hydromagmatic eruptions, Geology 43(3), 239–242.

1015 Lorenz, V., 1974. Vesiculated tuffs and associated features. Sedimentology, 21(2), 273-291.

1016 Lorenz, V. (1986), On the growth of maars and diatremes and its relevance to the formation of
1017 tuff rings, Bulletin of Volcanology 48(5), 265–274.

1018 Lorenz, V. (2003), Maar-diatreme volcanoes, their formation, and their setting in hard-rock or
1019 soft-rock environments, Geolines 15, 72–83.

1020 Mangan, M. & Cashman, K. (1996), The structure of basaltic scoria and reticulite and
1021 inferences for vesiculation, foam formation, and fragmentation in lava fountains, Journal of
1022 Volcanology and Geothermal Research 73(1- 2), 1–18.

1023 Mangan, M. & Sisson, T. (2000), Delayed, disequilibrium degassing in rhyolite magma:
1024 decompression experiments and implications for explosive volcanism, Earth and Planetary
1025 Science Letters 183(3), 441–455.

1026 Mangan, M. T., Cashman, K. V. & Swanson, D. A. (2014), The dynamics of Hawaiian-style
1027 eruptions: a century of study, in Poland, MP and Takahashi, TJ and Landowski, CM, ed.,
1028 'Characteristics of Hawaiian volcanoes', US Geological Survey, pp. 323–354.

1029 Mastin, L. (2001), A simple calculator of ballistic trajectories for blocks ejected during
1030 volcanic eruptions, US Geological Survey Open File Report 2001-45.

1031 Mastin, L. G. (1997), Evidence for water influx from a caldera lake during the explosive
1032 hydromagmatic eruption of 1790, Kilauea volcano, Hawaii, Journal of Geophysical Research:
1033 Solid Earth 102(B9), 20093–20109.

1034 Mastin, L. G. (2007), Generation of fine hydromagmatic ash by growth and disintegration of
1035 glassy rinds, Journal of Geophysical Research: Solid Earth 112, B02203.

1036 Mastin, L. G., Christiansen, R. L., Thornber, C., Lowenstern, J. & Beeson, M. (2004), What
1037 makes hydromagmatic eruptions violent? Some insights from the Keanakako'i Ash, Kilauea
1038 Volcano, Hawai'i, Journal of Volcanology and Geothermal Research 137(1), 15–31.

1039 Moore, J. (1967), Base surge in recent volcanic eruptions, Bulletin volcanologique 30(1), 337–
1040 363.

1041 Murtagh, R. M. & White, J. D. (2013), Pyroclast characteristics of a subaqueous to emergent
1042 Surtseyan eruption, Black Point volcano, California, Journal of Volcanology and Geothermal
1043 Research 267, 75–91.

1044 Murtagh, R. M., White, J. D. & Sohn, Y. K. (2011), Pyroclast textures of the Ilchulbong 'wet'
1045 tuff cone, Jeju Island, South Korea, Journal of Volcanology and Geothermal Research 201(1),
1046 385–396.

1047 Németh, K. & Cronin, S. J. (2011), Drivers of explosivity and elevated hazard in basaltic fissure
1048 eruptions: the 1913 eruption of Ambrym Volcano, Vanuatu (SW-Pacific), Journal of
1049 volcanology and geothermal research 201(1), 194– 209.

1050 Németh, K. & Kereszturi, G. (2015), Monogenetic volcanism: personal views and discussion,
1051 International Journal of Earth Sciences 104(8), 2131–2146.

1052 Németh, K., Cronin, S. J., Charley, D., Harrison, M. & Garae, E. (2006), Exploding lakes in
1053 Vanuatu-" Surtseyan- style" eruptions witnessed on Ambae Island, Episodes 29(2), 87.

1054 Németh, K., Cronin, S. J., Smith, I. E. & Flores, J. A. (2012), Amplified hazard of small-volume
1055 monogenetic eruptions due to environmental controls, Orakei Basin, Auckland Volcanic Field,
1056 New Zealand, Bulletin of volcanology 74(9), 2121–2137.

1057 Ólafsson, J. (1979), Physical characteristics of lake Mývatn and river Laxá, Oikos pp. 38–66.
1058 Þórarinsson, S. (1967), Surtsey: the new island in the North Atlantic, Viking Press.

1059 Parcheta, C., Houghton, B. & Swanson, D. (2013), Contrasting patterns of vesiculation in low,
1060 intermediate, and high Hawaiian fountains: a case study of the 1969 Mauna Ulu eruption,
1061 Journal of Volcanology and Geothermal Research 255, 79–89.

1062 Parfitt, E. A. (1998), A study of clast size distribution, ash deposition and fragmentation in a
1063 Hawaiian-style volcanic eruption, Journal of Volcanology and Geothermal Research 84(3),
1064 197–208.

1065 Patel, A., Manga, M., Carey, R.J. and Degruyter, W., (2013). Effects of thermal quenching on
1066 mechanical properties of pyroclasts, Journal of Volcanology and Geothermal Research, 258,
1067 24-30.

1068 Peckover, R., Buchanan, D. & Ashby, D. (1973), Fuel–coolant interactions in submarine
1069 vulcanism, Nature 245, 307-308.

1070 Pedrazzi, D., Martí, J. & Geyer, A. (2013), Stratigraphy, sedimentology and eruptive
1071 mechanisms in the tuff cone of El Golfo (Lanzarote, Canary Islands), Bulletin of volcanology
1072 75(7), 1–17.

1073 Pioli, L., Azzopardi, B. & Cashman, K. (2009), Controls on the explosivity of scoria cone
1074 eruptions: Magma segregation at conduit junctions, Journal of Volcanology and Geothermal
1075 Research 186(3), 407–415.

1076 Pioli, L., Erlund, E., Johnson, E., Cashman, K., Wallace, P., Rosi, M. & Granados, H. D.
1077 (2008), Explosive dynamics of violent Strombolian eruptions: the eruption of Parícutin
1078 Volcano 1943–1952 (Mexico), Earth and Planetary Science Letters 271(1), 359–368.

1079 Porritt, L. A., Russell, J. K. & Quane, S. L. (2012), Pele's tears and spheres: Examples from
1080 Kilauea Iki, Earth and Planetary Science Letters 333, 171–180.

1081 Pyle, D. M. (1989), The thickness, volume and grainsize of tephra fall deposits, Bulletin of
1082 Volcanology 51(1), 1–15.

1083 Rausch, J., Grobéty, B. & Vonlanthen, P. (2015), Eifel maars: Quantitative shape
1084 characterization of juvenile ash particles (Eifel Volcanic Field, Germany), Journal of
1085 Volcanology and Geothermal Research 291, 86–100.

1086 Ross, P.S. & White, J. D. (2012), Quantification of vesicle characteristics in some diatreme-
1087 filling deposits, and the explosivity levels of magma–water interactions within diatremes,
1088 Journal of Volcanology and Geothermal Research 245, 55–67.

1089 Rust, A. & Cashman, K. (2011), Permeability controls on expansion and size distributions of
1090 pyroclasts, Journal of Geophysical Research: Solid Earth 116, B11202.

1091 Sæmundsson, K. (1991), Jardfrædi Kröflukerfisins, in Garðarsson, A. and Einarsson, Á., ed.,
1092 'Náttúra Mývatns', 662, Hid íslenska Náttúrufrædifélag, Reykjavík, pp. 24–95.

1093 Schipper, C. I. & White, J. D. (2016), Magma-slurry interaction in Surtseyan eruptions,
1094 Geology, G37480–1.

1095 Schipper, C. I., White, J. D. L., Zimanowski, B., Büttner, R., Sonder, I., and Schmid, A., 2011,
1096 Experimental interaction of magma and "dirty" coolants: Earth and Planetary Science Letters,
1097 303, 3-4, 323-336.

1098 Schmid, A., Sonder, I., Seegelken, R., Zimanowski, B., Büttner, R., Gudmundsson, M. T., and
1099 Oddsson, B., 2010, Experiments on the heat discharge at the dynamic magma-water-interface:
1100 Geophysical Research Letters, 37, 20, L20311.

1101 Self, S., Sparks, R., Booth, B. & Walker, G. (1974), The 1973 Heimaey strombolian scoria
1102 deposit, Iceland, Geological Magazine 111(06), 539–548.

1103 Sheridan, M. F. & Wohletz, K. H. (1983), Hydrovolcanism: basic considerations and review,
1104 Journal of Volcanology and Geothermal Research 17(1), 1–29.

1105 Sohn, Y. K. (1996), Hydrovolcanic processes forming basaltic tuff rings and cones on Cheju
1106 Island, Korea, Geological Society of America Bulletin 108(10), 1199–1211.

1107 Sohn, Y. K. & Chough, S. K. (1993), The Udo tuff cone, Cheju Island, South Korea:
1108 transformation of pyroclastic fall into debris fall and grain flow on a steep volcanic cone slope,
1109 Sedimentology 40(4), 769–786.

1110 Sohn, Y. K. & Park, K. H. (2005), Composite tuff ring/cone complexes in Jeju Island, Korea:
1111 possible consequences of substrate collapse and vent migration, Journal of Volcanology and
1112 Geothermal Research 141(1), 157–175.

1113 Solgevik, H., Mattsson, H. B. & Hermelin, O. (2007), Growth of an emergent tuff cone:
1114 fragmentation and depositional processes recorded in the Capelas tuff cone, São Miguel,
1115 Azores, Journal of Volcanology and Geothermal Research 159(1), 246–266.

1116 Stovall, W. K., Houghton, B. F., Hammer, J. E., Fagents, S. A. & Swanson, D. A. (2012),
1117 Vesiculation of high fountaining Hawaiian eruptions: Episodes 15 and 16 of 1959 Kilauea Iki,
1118 Bulletin of volcanology 74(2), 441–455.

1119 Stovall, W. K., Houghton, B., Gonnermann, H., Fagents, S. & Swanson, D. (2011), Eruption
1120 dynamics of Hawaiian-style fountains: the case study of episode 1 of the Kilauea Iki 1959
1121 eruption, Bulletin of volcanology 73(5), 511– 529.

1122 Þórarinsson, S. (1952), Hverfjall I., Náttúrufrædingurinn, 22, 113-129.

1123 Þórarinsson, S. (1979), The postglacial history of the Mývatn area, Oikos 17–28.

1124 Thordarson, T. & Höskuldsson, Á. (2008), Postglacial volcanism in Iceland, Jökull 58, 197–
1125 228.

1126 Toramaru, A. (2006), BND (bubble number density) decompression rate meter for explosive
1127 volcanic eruptions, Journal of Volcanology and Geothermal Research 154(3), 303–316.

1128 Valentine, G. A., Krier, D. J., Perry, F. V. & Heiken, G. (2007), Eruptive and geomorphic
1129 processes at the Lathrop Wells scoria cone volcano, Journal of Volcanology and Geothermal
1130 Research 161(1), 57–80.

1131 Valentine, G. A., Krier, D., Perry, F. V. & Heiken, G. (2005), Scoria cone construction
1132 mechanisms, Lathrop Wells volcano, southern Nevada, USA, Geology 33(8), 629–632.

1133 Valentine, G. A., Sottili, G., Palladino, D. M. & Taddeucci, J. (2015), Tephra ring interpretation
1134 in light of evolving maar–diatreme concepts: Stracciacappa maar (central Italy), Journal of
1135 Volcanology and Geothermal Research 308, 19–29.

1136 Van Otterloo, J., Cas, R. A. & Sheard, M. J. (2013), Eruption processes and deposit
1137 characteristics at the monogenetic Mt. Gambier Volcanic Complex, SE Australia: implications
1138 for alternating magmatic and phreatomagmatic activity, Bulletin of volcanology 75(8), 1–21.

1139 Van Otterloo, J., Cas, R.A. and Scutter, C.R. (2015). The fracture behaviour of volcanic glass
1140 and relevance to quench fragmentation during formation of hyaloclastite and
1141 phreatomagmatism, Earth Science Reviews, 151, 79-116.

1142 Vaughan, R. G. & Webley, P. W. (2010), Satellite observations of a surtseyan eruption: Hunga
1143 Ha'apai, Tonga, Journal of Volcanology and Geothermal Research 198(1), 177–186.

1144 Walker, G. (1971), Grain-size characteristics of pyroclastic deposits, The Journal of Geology
1145 79(6), 696–714.

1146 Walker, G. (1973), Explosive volcanic eruptions: A new classification scheme, Geologische
1147 Rundschau 62(2), 431–446.

1148 Walker, G. & Croasdale, R. (1971), Characteristics of some basaltic pyroclastics, Bulletin
1149 volcanologique 35(2), 303– 317.

1150 Waters, A. C. & Fisher, R. V. (1971), Base surges and their deposits: Capelinhos and Taal
1151 volcanoes, Journal of Geophysical Research 76(23), 5596–5614.

1152 White, J. & Valentine, G. (2015), Magmatic versus phreatomagmatic fragmentation: Absence
1153 of evidence is not evidence of absence, in '2015 AGU Fall Meeting Abstracts', AGU, V33B–
1154 3108.

1155 White, J. D. (1996), Impure coolants and interaction dynamics of phreatomagmatic eruptions,
1156 Journal of Volcanology and Geothermal Research 74(3), 155–170.

1157 White, J. D. & Ross, P.-S. (2011), Maar-diatreme volcanoes: a review, Journal of Volcanology
1158 and Geothermal Research 201(1), 1–29.

1159 White, J. D. & Schmincke, H. (1999), Phreatomagmatic eruptive and depositional processes
1160 during the 1949 eruption on La Palma (Canary Islands), Journal of Volcanology and
1161 Geothermal Research 94(1), 283–304.

1162 Witt, T. & Walter, T. (2016), Dynamics at the Holuhraun eruption based on high speed video
1163 data analysis, in 'EGU General Assembly Conference Abstracts', Vol. 18, 16440.

1164 Wohletz, K. (1983), Mechanisms of hydrovolcanic pyroclast formation: Grainsize, SEM, and
1165 experimental studies, Journal of Volcanology and Geothermal Research 17(1-4), 31–63.

1166 Wohletz, K. & Sheridan, M. (1983), Hydrovolcanic Explosions 2. Evolution of baslatic tuff
1167 rings and tuff cones, American Journal of Science 283(5), 385–413.

1168 Wohletz, K. H. (1986), Explosive magma-water interactions: Thermodynamics, explosion
1169 mechanisms, and field studies, Bulletin of Volcanology 48(5), 245–264.

1170 Wright, H., Cashman, K., Mothes, P., Hall, M., Gorki R., A. & Le Pennec, J. (2012), Estimating
1171 rates of decompression from textures of erupted ash particles produced by 1999-2006 eruptions
1172 of Tungurahua volcano, Ecuador, Geology 40(7), 619–622.

1173 Zimanowski, B., Büttner, R., Dellino, P., White, J.D.L. and Wohletz, K.H., (2015), Chapter 26
1174 - Magma Water Interaction and Phreatomagmatic Fragmentation, in H. Sigurdsson, ed., 'The
1175 Encyclopedia of Volcanoes (Second Edition)', Academic Press, Amsterdam, 473–484.

1176 Zimanowski, B., Büttner, R., Lorenz, V. & Häfele, H.-G. (1997), Fragmentation of basaltic
1177 melt in the course of explosive volcanism, Journal of Geophysical Research: Solid Earth
1178 102(B1), 803–814.

1179 Zimanowski, B., Fröhlich, G. & Lorenz, V. (1991), Quantitative experiments on
1180 phreatomagmatic explosions, Journal of Volcanology and Geothermal Research 48(3), 341–
1181 358.

1182 Zimanowski, B., Wohletz, K., Dellino, P. & Büttner, R. (2003), The volcanic ash problem,
1183 Journal of Volcanology and Geothermal Research 122(1-2), 1–5.

1184

1185

Figure Captions

Figure 1: Bubble number densities (log BND; m^{-3}) and vesicularities (2D) for hydromagmatic (blue; sample site 2.3) and magmatic (red; sample site Q1) clasts from the Hverfjall Fires, measured from 1–2 mm (circles), 4–8 mm (diamond) and 16–32 mm (triangle) particle sizes. A selection of datapoints are annotated with the corresponding backscattered electron SEM images for illustration. The white scalebars on all SEM images are 0.5 mm. Shaded fields highlight the ranges of BNDs and vesicularities from other hydromagmatic (blue) and magmatic (red) basaltic eruptions: Black Point (US; Murtagh and White, 2013), Ilchulbong tuff cone (Korea; Murtagh et al., 2011), Keanakako'i (Hawaii; Mastin et al., 2004), Capelas (Azores; Mattsson et al., 2010); Kilauea Iki and Mauna Ulu eruptions of Kilauea (Hawaii; Stovall et al., 2012; Porritt et al., 2012; Parcheta et al., 2013). For Kilauea Iki, cores and rims from single clasts are shown individually where analysed separately (Stovall et al., 2012). Vesicularity and BND ranges for the Coombs Hill diatreme are show by the grey shaded field (Ross and White, 2012). The range of BNDs for the 2011 Grímsvötn deposits, for which vesicularity data are not available, are shown by the blue arrowed lines (Liu et al., 2015a). The range of vesicularities for the lava fountain deposits of the 2000 and 2006 Etna (Italy; Polacci et al., 2009) and Pu'u'O'o-Kupaianaha (Kilauea; Mangan et al., 1993) eruptions are shown by the red arrowed lines, for which Nv data are not available.

Figure 2: Study area; (a) Location of the Krafla Volcanic System (KVS) in the larger tectonic setting of Iceland; (b) Regional scale map of the KVS, showing sampling locations and corresponding labels (black symbols; Table S2, isopachs for the hydromagmatic fall deposit (*redrawn from Mattsson and Höskuldsson, 2011), and the locations of lava flows erupted during the Hverfjall Fires (red shaded regions; from Saemundsson, 1991). Groundwater flow

vectors are depicted by the blue arrows (redrawn from Einarsson, 2004). The previous extent of the proto Lake Mývatn is shown by the grey dashed region. (c) Detailed map of area enclosed by black rectangle in Fig. 2, showing the locations of sampling sites that are discussed in the text superimposed onto GoogleEarth topographic imagery.

Figure 3: Sedimentary features of the hydromagmatic deposits; (a) The Hverfjall tuff ring, viewed from the NW shore of Lake Mývatn; (b) Hverfjall deposits lie stratigraphically above the widespread Hekla-3 silicic ash layer, separated by 1–3 cm of soil [site 9.3]; (c) Weathering of base surge deposits has produced characteristic circular erosional features [site 8.9]; (d) Long wavelength undulatory bedding in surge deposits [site 8.9]. The wavelength of bedding undulations varies between 2.5 and 3.1 m, with a wave height of ~11 cm. Similar base surge deposits at Taal, Philippines, have a slightly longer wavelength of 5.5 m and a wave height of 70 cm at the same distance from the respective vent location (Waters and Fisher, 1971); (e) Accretionary lapilli tuff in the upper surge units [site 8.9]; (f) Poorly-sorted massive lapilli-tuff in lower surge units [site 8.9]; (g) Impact structure showing surrounding soft sediment deformation; (h) Tree mold in lower surge unit [site 4.1]; (i) Flute marks on the underside of beds in the stratified lapilli tuff units [site 5.8].

Figure 4: Deposit thinning as a function of distance, expressed in the form of the $\sqrt{area}$ of the enclosing isopach. Circular symbols correspond to the isopach contours for the hydromagmatic deposit (from Mattsson and Höskuldsson, 2011), coloured according to whether the thickness includes both fall and surge units (orange) or fall only (blue). The thinning relationship can be well described by a two-segment exponential, with the inflection point occurring at the maximum distal extent of the surge deposits. Crosses correspond to fall/surge thickness measurements from individual outcrops made during this study, with their relative position on

the x-axis determined by the Area$^{1/2}$ of their enclosing isopach. Again, symbol colour indicates whether surge deposits were present or absent in the sequence. When fall thickness is decoupled from total thickness (fall + surge), the thinning relationship can be described by a single-segment exponential.

Figure 5: Stratigraphic sections through the deposits of the Hverfjall Fires (both magmatic and hydromagmatic) at distances of 1.6 km [site 8.9] to 19 km [site 6.4] from the Hverfjall vent. Background shading highlights units that have been correlated between sections, including hydromagmatic fall (blue), massive lapilli tuff (green), magmatic scoria lapilli (red), and lava flow (pale red). All units that do not have a shaded background correspond to hydromagmatic base surge deposits.

Figure 6: Crystal and bubble textures in hydromagmatic pyroclasts [sample site 2.3]. Skeletal morphologies of (a) olivine [ol], (b) plagioclase [plag], and minor clinopyroxene phenocryst phases are indicative of rapid growth; (c) Composite clasts are common, particularly for coarse ash and lapilli, where recycled crystalline lithics (cognate and/or accessory) are incorporated into juvenile sideromelane clasts. The boundaries between recycled clasts and the host matrix is often sharp, and demarcated by (d) vesicle void space, or (e) rims of oxide crystals; (f) Although most bubbles are preserved as spherical vesicles, some pyroclasts preserve sheared and deformed bubbles indicative of rapid quenching faster than the relaxation time of low viscosity basaltic melt. Deformation often occurs around phenocryst phases; (g, h) Particles sometimes exhibit either partial or complete fluidal rims, characteristic of viscous deformation.

Figure 7: Grain size distributions (GSDs) for the deposits of the Hverfjall Fires. Note that GSDs refer to size distributions at specific locations, while total grain size distributions

(TGSDs) incorporate many individual GSDs from different locations; (a) GSDs for the Hverfjall hydromagmatic fall unit (coloured according to distance from the Hverfjall vent) and the magmatic scoria deposit (black and grey lines, where the black line represents the full reconstructed proximal GSD including bomb-sized clasts). Dashed lines correspond to the GSDs of mixed deposits of both hydromagmatic and magmatic pyroclasts, and are typically bimodal; (b) TGSDs for Hverfjall (dark blue symbols) and Jan Mayan (grey symbols; Gjerlow et al., 2015) are compared to distal hydromagmatic GSDs for Hverfjall (site 6.4; light blue symbols) and Grímsvötn, Iceland (50–115 km from the 2011 vent; Liu et al., 2015a). A proximal magmatic GSD for Jardbadsholar (site Q1; red symbols) is compared to the TGSD for Kīlauea Iki, Hawaii (Parfitt, 1998). Grey shaded field highlights the range of typical GSDs for proximal deposits from other hydromagmatic eruptions (<1 km from the vent; from Liu et al., 2015a).

Figure 8: Variation in the relative proportions of dense glass fragments (blue), vesicular particles (green), shards (red), microcrystalline grains (purple), free crystals and lithic grains (black), as a function of grain size and distance from the vent. (a) Magmatic deposits at 0.4 (cone; site Q1) and 0.5 km (site 6.3) dispersal distance, over grain sizes of 0φ (1–2 mm) to 4φ (0.063 to 0.125 mm); (b) Hydromagmatic fall deposits at 1 (site 2.3), 3.5 (site 6.3), 4.5 (site 9.3) and 17 km (site 7.5) dispersal distance, over grain sizes of 0φ (1–2 mm) to 6φ (0.016 to 0.032 mm). Inset images: Representative backscattered electron SEM images of each component class.

Figure 9: Average density (and vesicularity) as a function of grain size, for magmatic (triangles) and hydromagmatic (circles) samples. Vesicularity is calculated assuming a dense rock equivalent of 2800 kg m^{-3}. Most error bars (1σ) are smaller than the symbol size.

Figure 10: Vesicle volume distributions (VVD; right column) for representative low, moderate and high vesicularity clasts from hydromagmatic (blue; site 2.3) and magmatic (red; site Q1) deposits. The corresponding vesicularities and bubble number densities for each clast are shown in Figure 1.

Figure 11: Comparison of grain size distributions (GSD; solid lines) and cumulative vesicle volume distributions (VVDs; dashed lines) for (a) magmatic and (b) hydromagmatic deposits. Shaded regions show the range of VVDs in other mafic eruptions for comparison; *Magmatic lava fountains: Kilauea Iki, Hawaii (Stovall et al., 2011; Stovall et al., 2012; Porritt et al., 2012); Hydromagmatic: Black Point, US (Murtagh and White, 2013), Capelas, Azores (Mattsson et al., 2010), and 2011 Grímsvötn, Iceland (Liu et al., 2015a).

Figure 12: (a) Total grain size distributions (TGSD) for the hydromagmatic fall and (c) GSD for a proximal magmatic scoria deposit [site Q1], showing the contributions of dense fragments (blue), vesicular particles (green), shards (red), microcrystalline grains (purple), and free crystals/lithics (black) to each size fraction (averaged over samples from a range of dispersal distances). Colour scheme is identical to Figure 8. The range and modal vesicle sizes from Figure 9 are annotated for comparison; (b) Total componentry distributions (TCDs) for hydromagmatic fall (left) and magmatic scoria (right), determined by weighting the componentry of individual grain size fractions by the total grain size distributions shown in (a) and (c).

Figure 13: Comparison of the relative proportions of dense fragments (black bars) and bubbly grains (shards and vesicular particles combined; pale grey bars) as a function of grain size, for

1311 the hydromagmatic deposits of the 2011 Grímsvötn (G; data from Liu et al., 2015a) and
1312 Hverfjall (HV; this study) eruptions. The data shown for each grain size represent averages of
1313 all samples of varying dispersal distance. The range of size fractions displayed is more
1314 restricted than shown in Figure 8, to enable comparison with the size range analysed for the
1315 Grímsvötn deposits.

Figure 1:

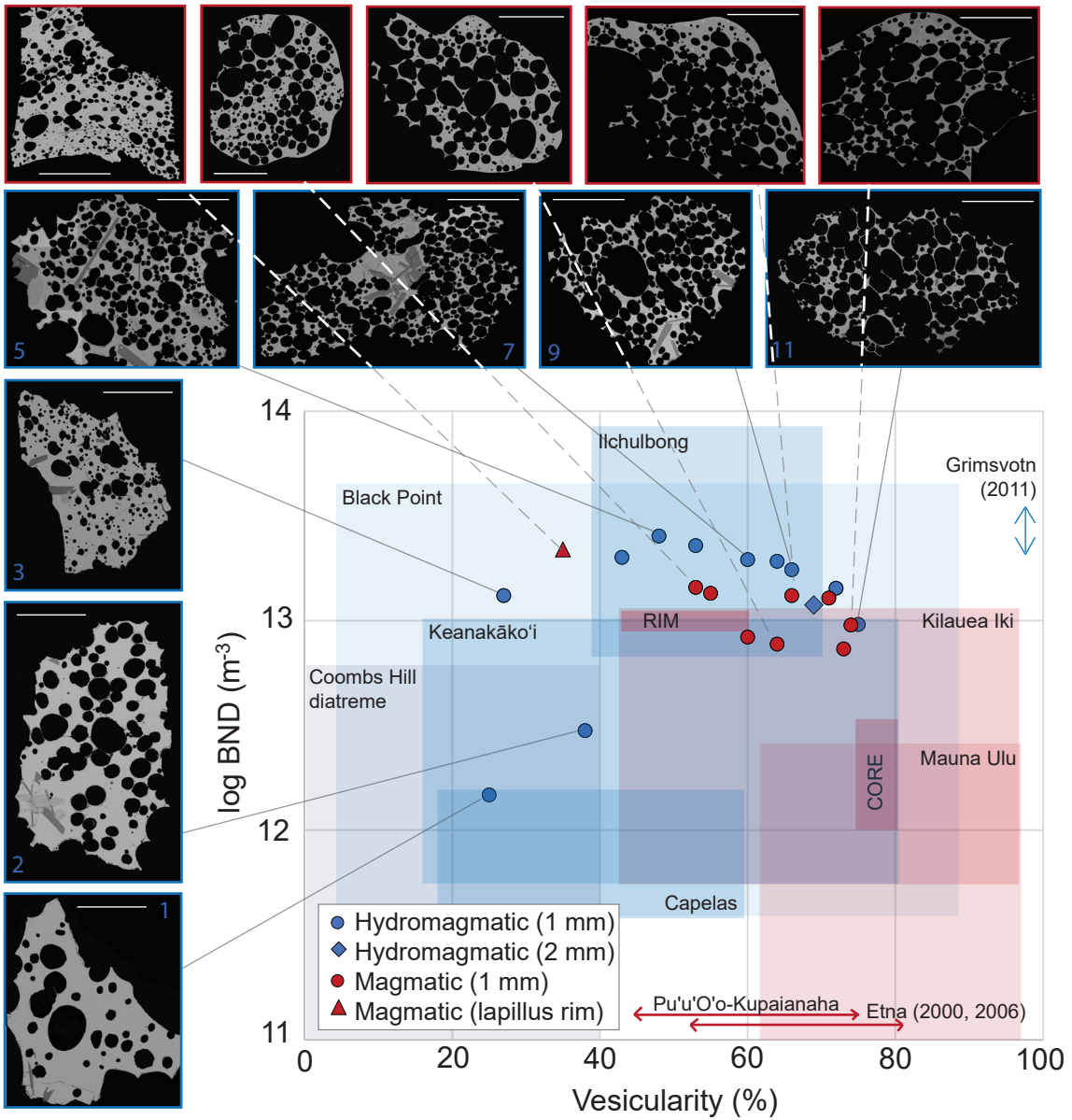
5
7
9
11
3
2
1
14
13
12
11
log BND (m-3)
0
20
40
60
80
100
Vesicularity (%)
Ilchulbong
Grimsvotn
(2011)
Black Point
Keanakāko'i
RIM
Kilauea Iki
Coombs Hill
diatreme
CORE
Mauna Ulu
Capelas
Hydromagmatic (1 mm)
Hydromagmatic (2 mm)
Magmatic (1 mm)
Magmatic (lapillus rim)
Pu'u'O'o-Kupaianaha
Etna (2000, 2006)

Figure 2:

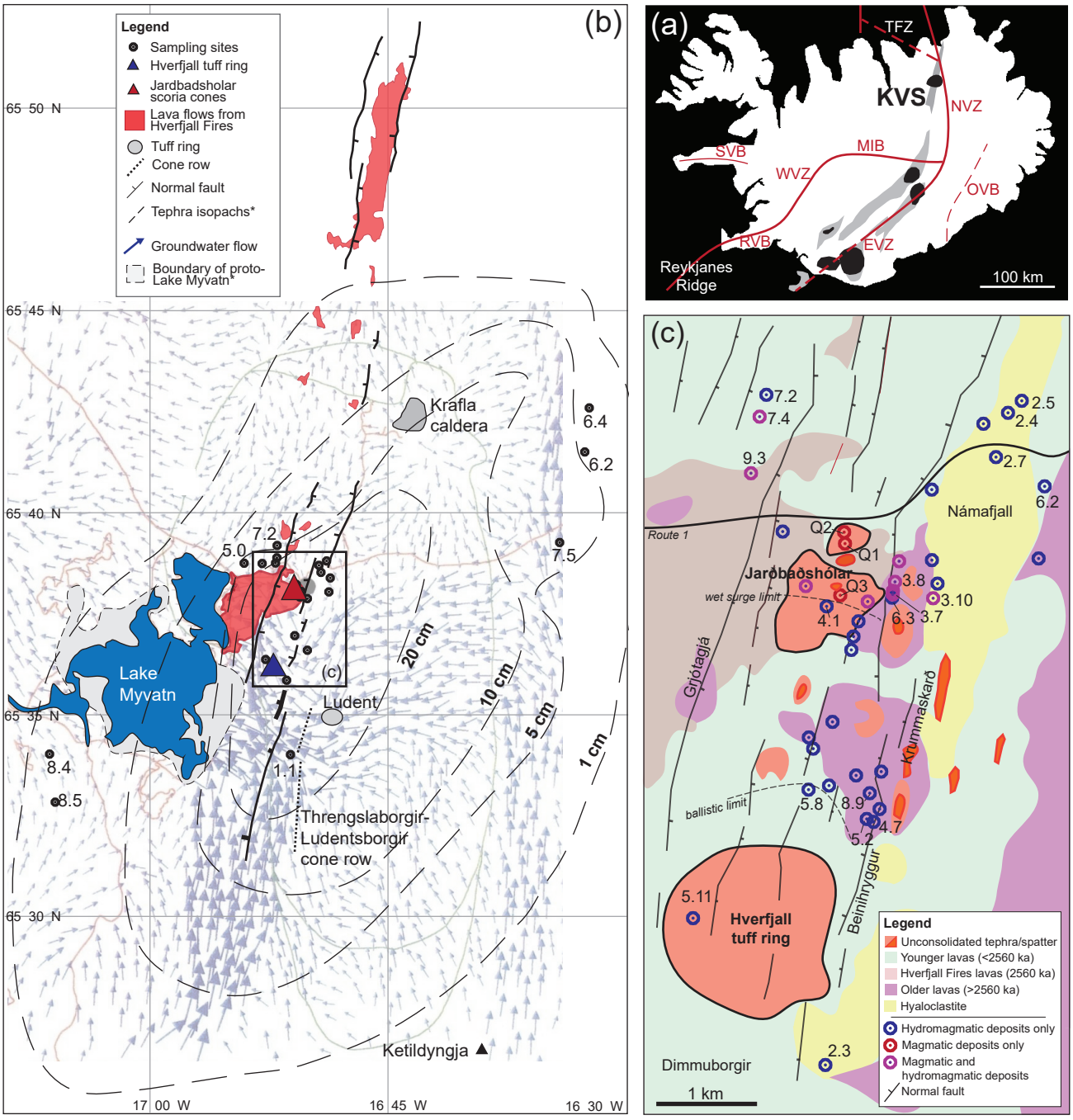
(b)
Legend
Sampling sites
Hverfjall tuff ring
Jardbadsholar scoria cones
Lava flows from Hverfjall Fires
Tuff ring
Cone row
Normal fault
Tephra isopachs*
Groundwater flow
Boundary of proto-Lake Myvatn*
65 50 N
65 45 N
65 40 N
65 35 N
65 30 N
17 00 W
16 45 W
16 30 W
Krafla caldera
Lake Myvatn
Ludent
Threngslaborgir-Ludentsborgir cone row
Ketildyngja
20 cm
10 cm
5 cm
1 cm
(c)
(a)
TFZ
KVS
NVZ
MIB
SVB
WVZ
OVB
RVB
EVZ
Reykjanes Ridge
100 km
(c)
Námafjall
Route 1
Jarðbaðshólar
wet surge limit
ballistic limit
Grjótagjá
Krummaskarð
Bæjarhryggur
Hverfjall tuff ring
Dimmuborgir
1 km
Legend
Unconsolidated tephra/spatter
Younger lavas (<2560 ka)
Hverfjall Fires lavas (2560 ka)
Older lavas (>2560 ka)
Hyaloclastite
Hydromagmatic deposits only
Magmatic deposits only
Magmatic and hydromagmatic deposits
Normal fault

Figure 3:

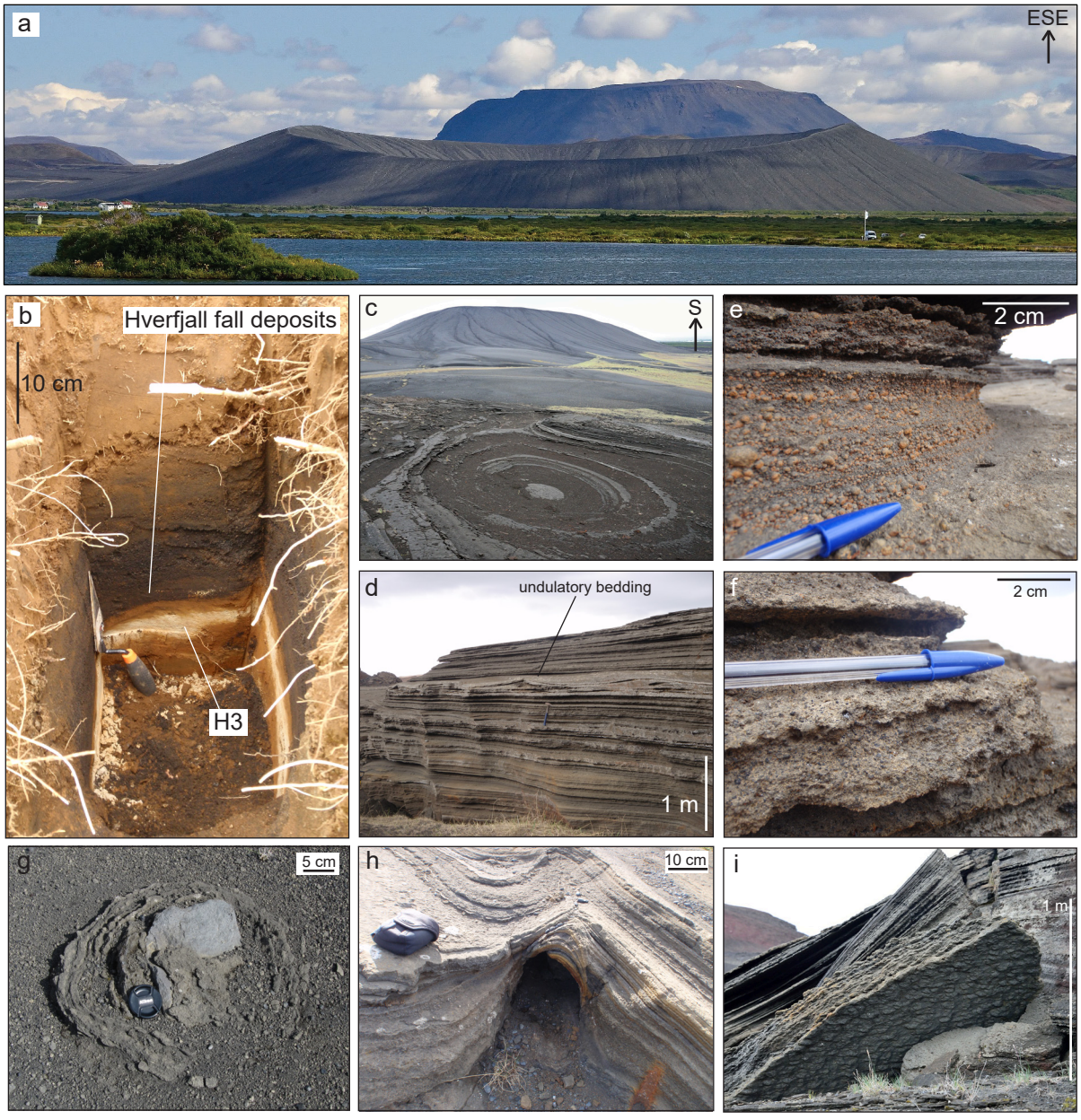
a
ESE
b
Hverfjall fall deposits
10 cm
H3
c
S
d
undulatory bedding
1 m
e
2 cm
f
2 cm
g
5 cm
h
10 cm
i
1 m

Figure 4:

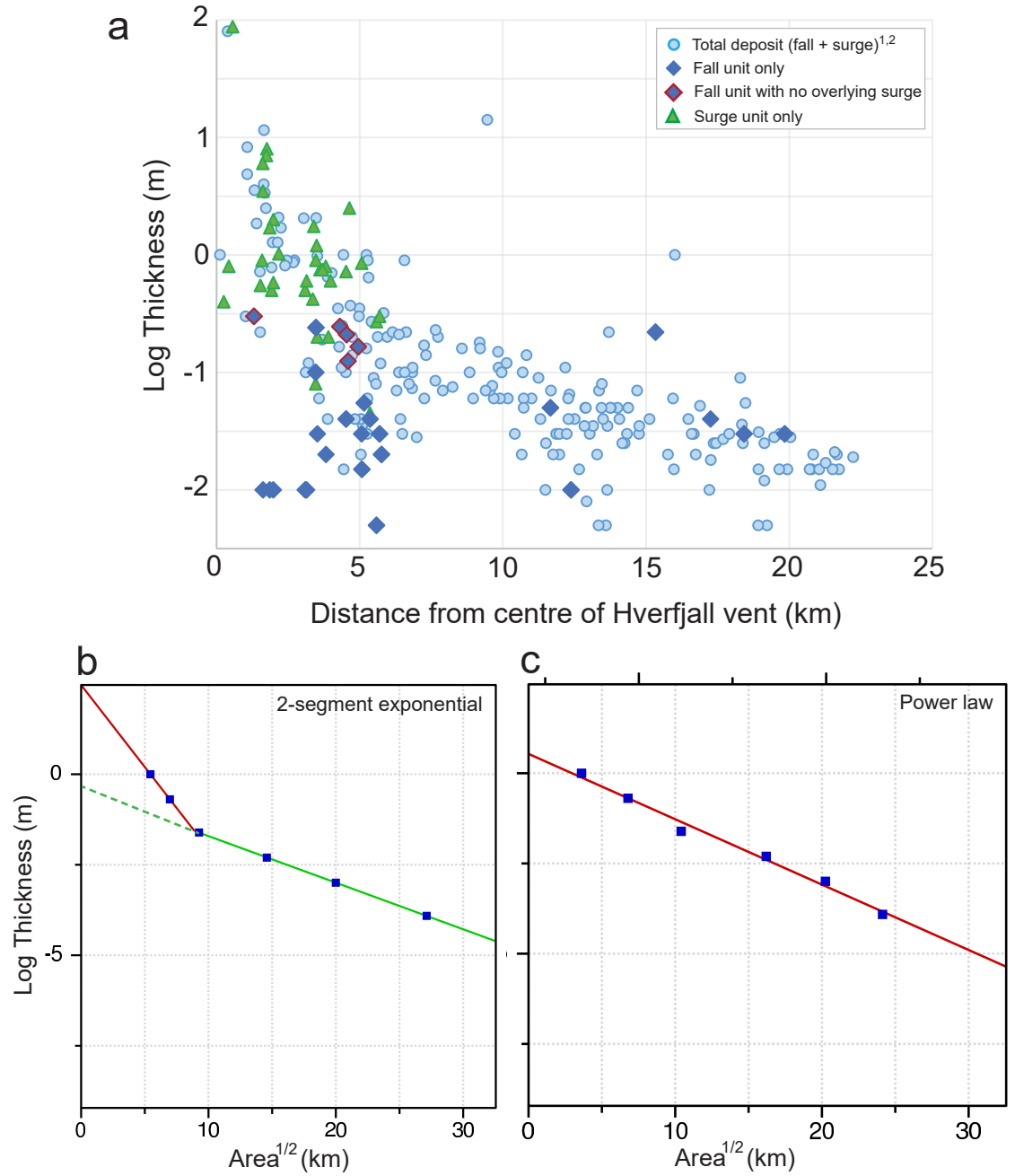
a
Total deposit (fall + surge)[1,2]
Fall unit only
Fall unit with no overlying surge
Surge unit only
Log Thickness (m)
Distance from centre of Hverfjall vent (km)
b
2-segment exponential
Log Thickness (m)
Area[1/2] (km)
c
Power law
Area[1/2] (km)

Figure 5:

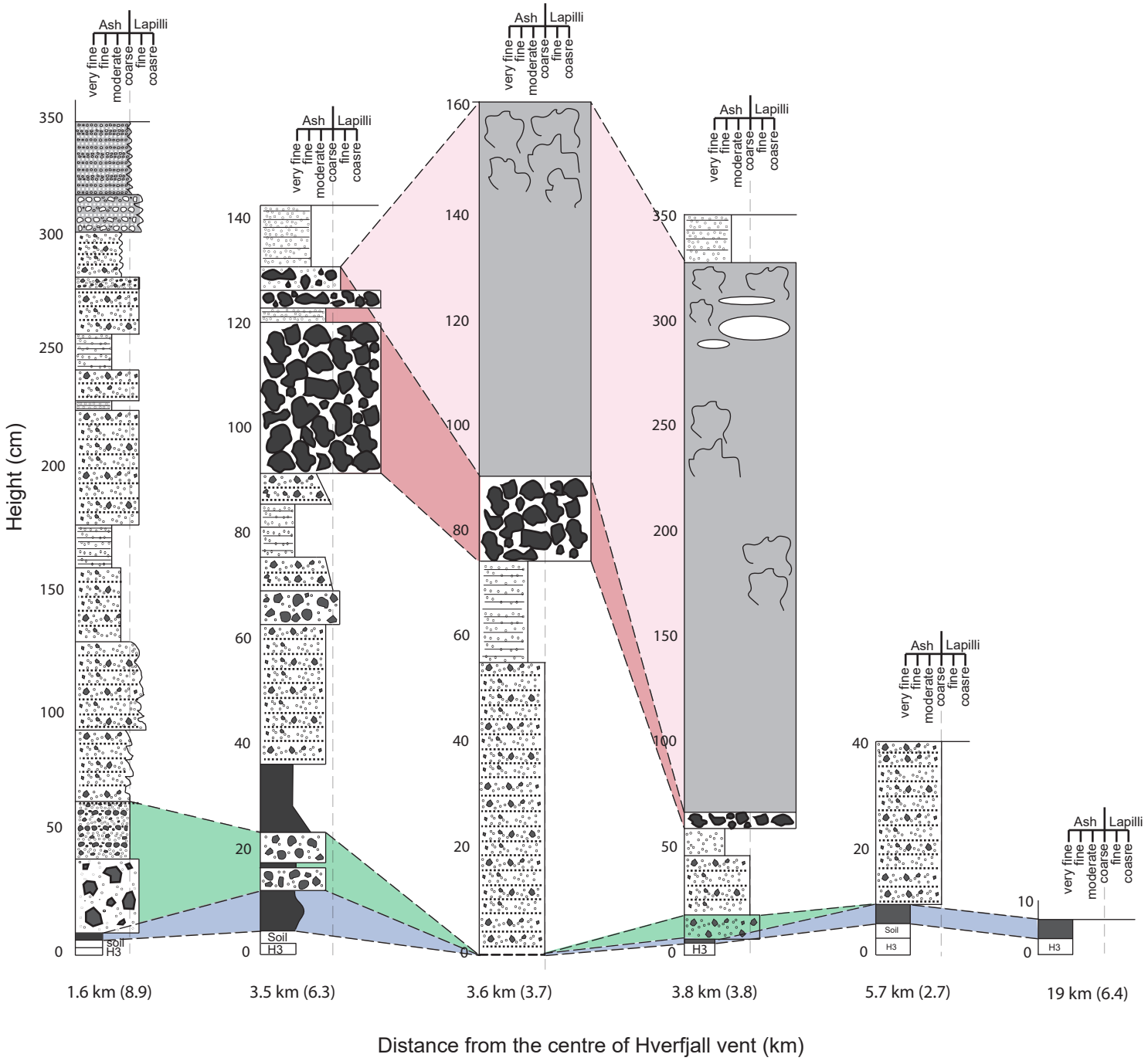

Table A: Description of stratigraphic units

	Description
	Unit 3: Magmatic airfall deposit
	Lava flow: Massive flow unit, with some vesicular scoriaceous regions (wavy symbols) or large vesicles (oval symbols), often in the uppermost part of the flow.
	Scoriaceous lapilli: Massive, clast-supported beds of fine to coarse lapilli, with minor interstitial ash. Lapilli are highly vesicular, and commonly show both fluidal and brittle fracture surfaces on individual clasts.
	Unit 2: Hydromagmatic surge deposits
	Accretionary tuff (Ac-T): Clast-supported thin cm-scale beds of spherical accretionary pellets and coated particles (<2 mm) separated by mm-scale fine ash laminae. Planar bedding.
	Accretionary lapilli-tuff (Ac-LT): Clast-supported beds of spherical accretionary pellets and coated particles (up to 1-2 cm) separated by cm-scale beds of thinly-laminated fine ash. Planar bedding.
	Finely stratified tuff (FS-T): Thinly-bedded to laminated fine-grained ash layers. Moderately to well-sorted, all clasts <1 mm. Cross-stratification/undulatory bedding is common.
	Stratified lapilli-tuff (S-LT): Clast-supported and moderately-sorted beds (~3-10 cm thick) of fine lapilli and coarse ash intercalated with internally stratified moderately coarse ash. Cross-stratification and undulatory bedding are often present within lapilli-poor layers.
	Crudely-stratified lapilli tuff (CS-LT): Angular fine lapilli (juvenile and dense lithic) within a moderately coarse ash matrix. Individual beds are ~5-10 cm in thickness, and show very crude normal grading. Poorly-sorted.
	Massive lapilli-tuff (M-LT): Thick massive beds, with little internal structure. Abundant angular fine lapilli and occasional bombs (juvenile and dense lithic) up to 8 cm in diameter, within a moderately coarse ash matrix. Very poorly sorted. Tree molds and bomb sags are common.
	Unit 1: Hydromagmatic airfall deposit
	Unconsolidated ash: Massive, unconsolidated deposit, comprising fine to very-fine ash. Well-sorted, with slight internal grading (fine-coarse-fine) in some exposures.

Figure 6:

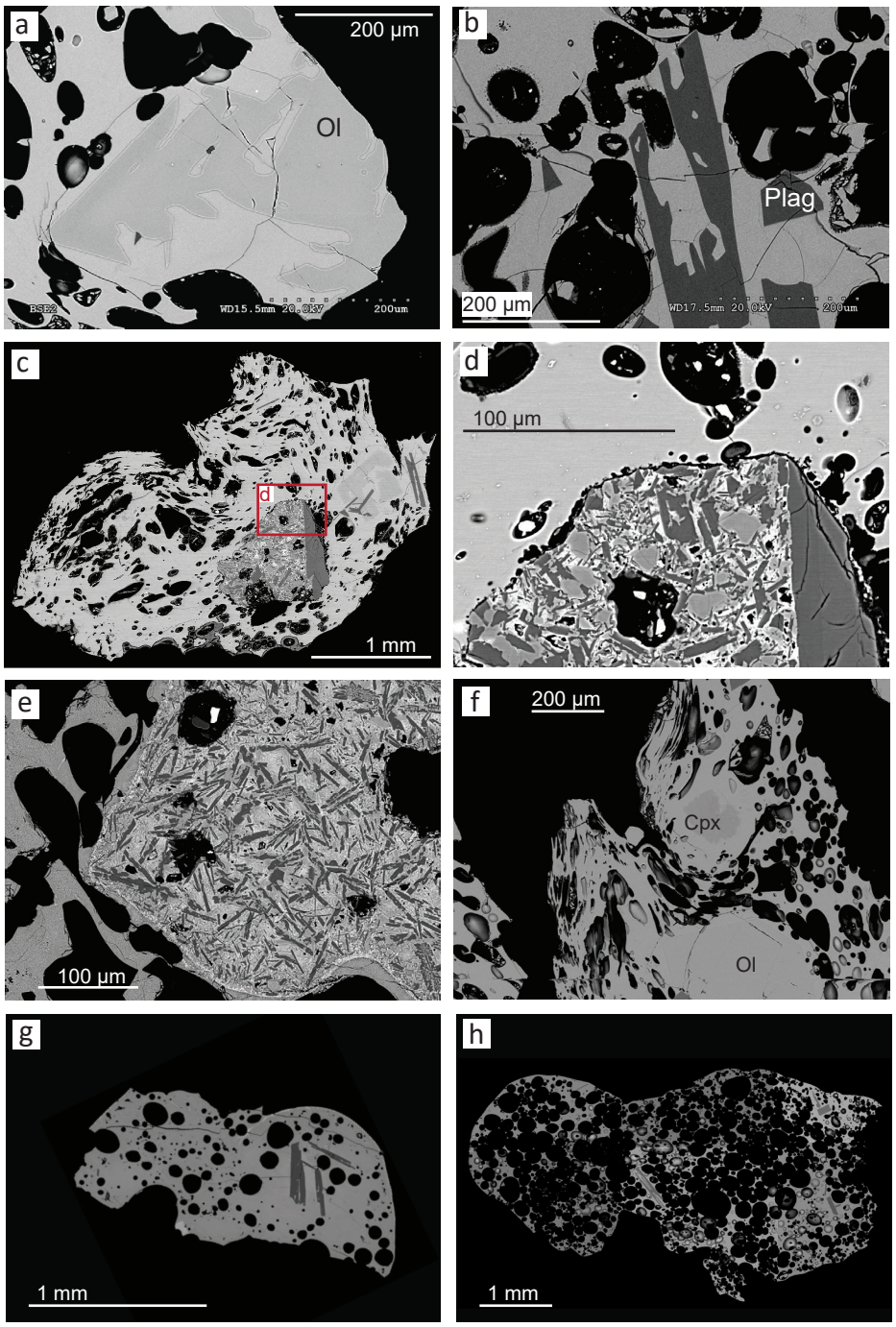
a
200 µm
Ol
b
Plag
200 µm
c
d
1 mm
d
100 µm
e
100 µm
f
200 µm
Cpx
Ol
g
1 mm
h
1 mm

Figure 7:

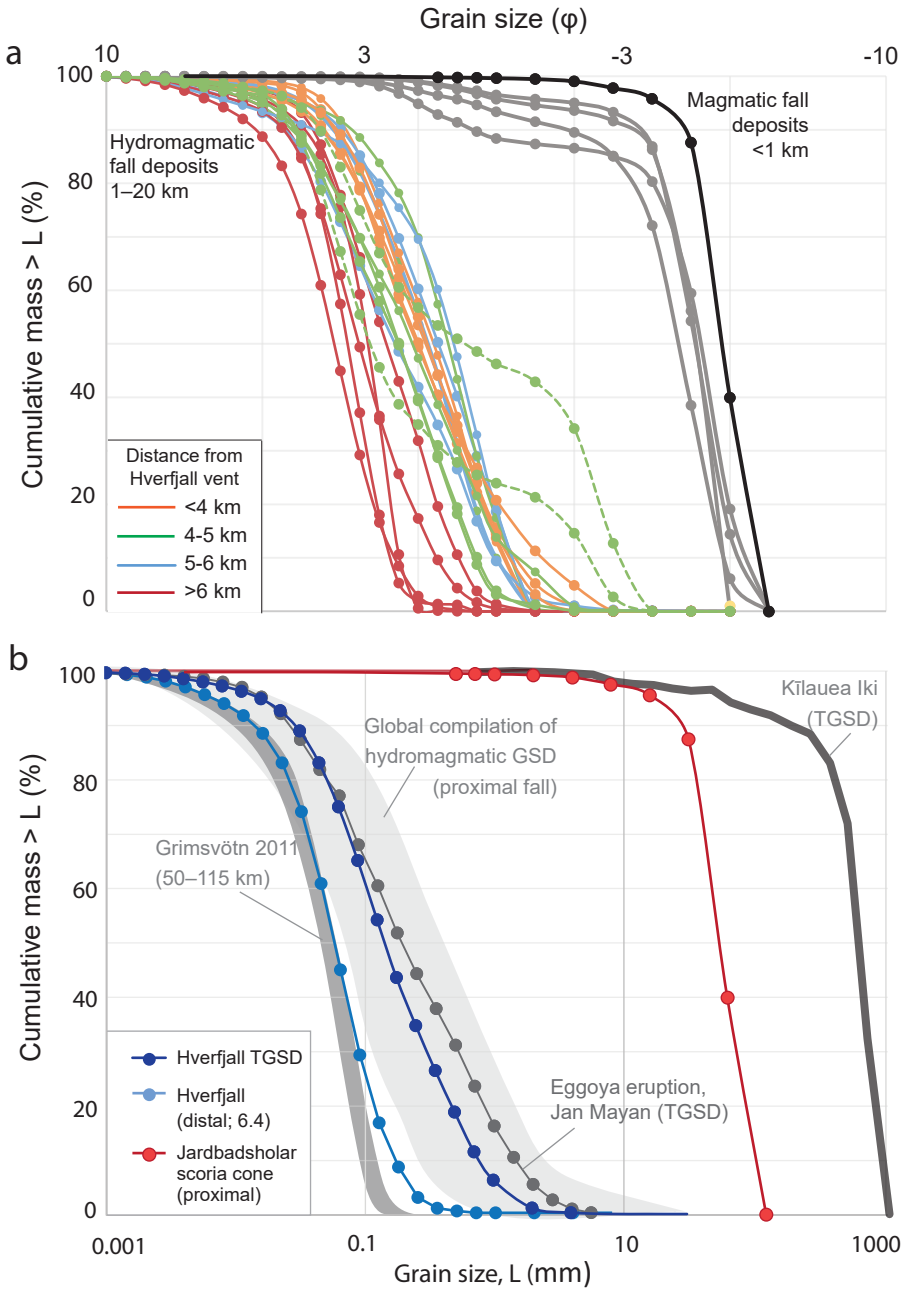
a
Grain size (φ)
10
3
-3
-10
100
80
60
40
20
0
Cumulative mass > L (%)
Hydromagmatic
fall deposits
1–20 km
Magmatic fall
deposits
<1 km
Distance from
Hverfjall vent
<4 km
4-5 km
5-6 km
>6 km
b
Kīlauea Iki
(TGSD)
Global compilation of
hydromagmatic GSD
(proximal fall)
Grimsvötn 2011
(50–115 km)
Eggoya eruption,
Jan Mayan (TGSD)
Hverfjall TGSD
Hverfjall
(distal; 6.4)
Jardbadsholar
scoria cone
(proximal)
0.001
0.1
10
1000
Grain size, L (mm)

Figure 8:

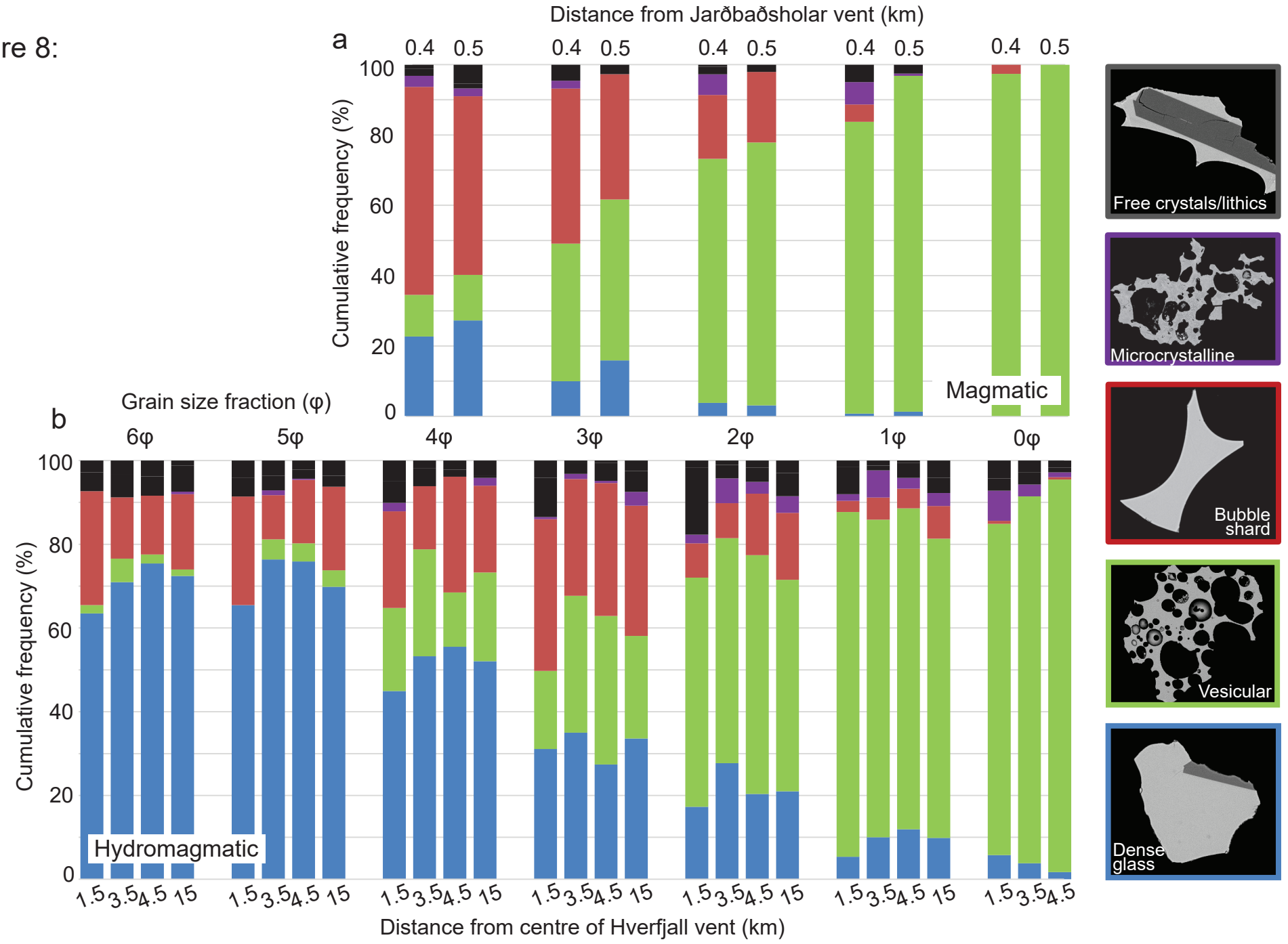
a
Distance from Jarðbaðsholar vent (km)
0.4
0.5
Cumulative frequency (%)
100
80
60
40
20
0
Magmatic
b
Grain size fraction (φ)
6φ
5φ
4φ
3φ
2φ
1φ
0φ
Hydromagmatic
1.5
3.5
4.5
15
Distance from centre of Hverfjall vent (km)
Free crystals/lithics
Microcrystalline
Bubble shard
Vesicular
Dense glass

Figure 9:

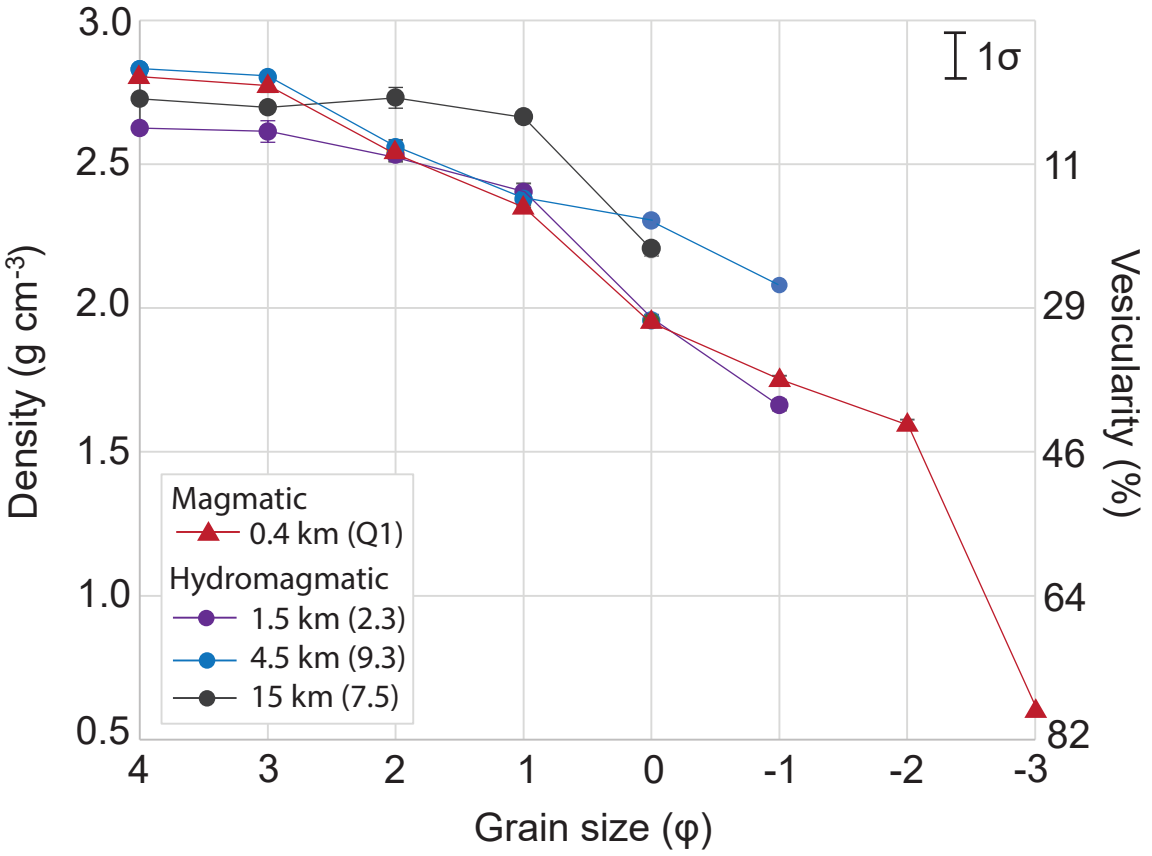
3.0
2.5
2.0
1.5
1.0
0.5
Density (g cm-3)
11
29
46
64
82
Vesicularity (%)
1σ
Magmatic
0.4 km (Q1)
Hydromagmatic
1.5 km (2.3)
4.5 km (9.3)
15 km (7.5)
4
3
2
1
0
-1
-2
-3
Grain size (φ)

Figure 10:

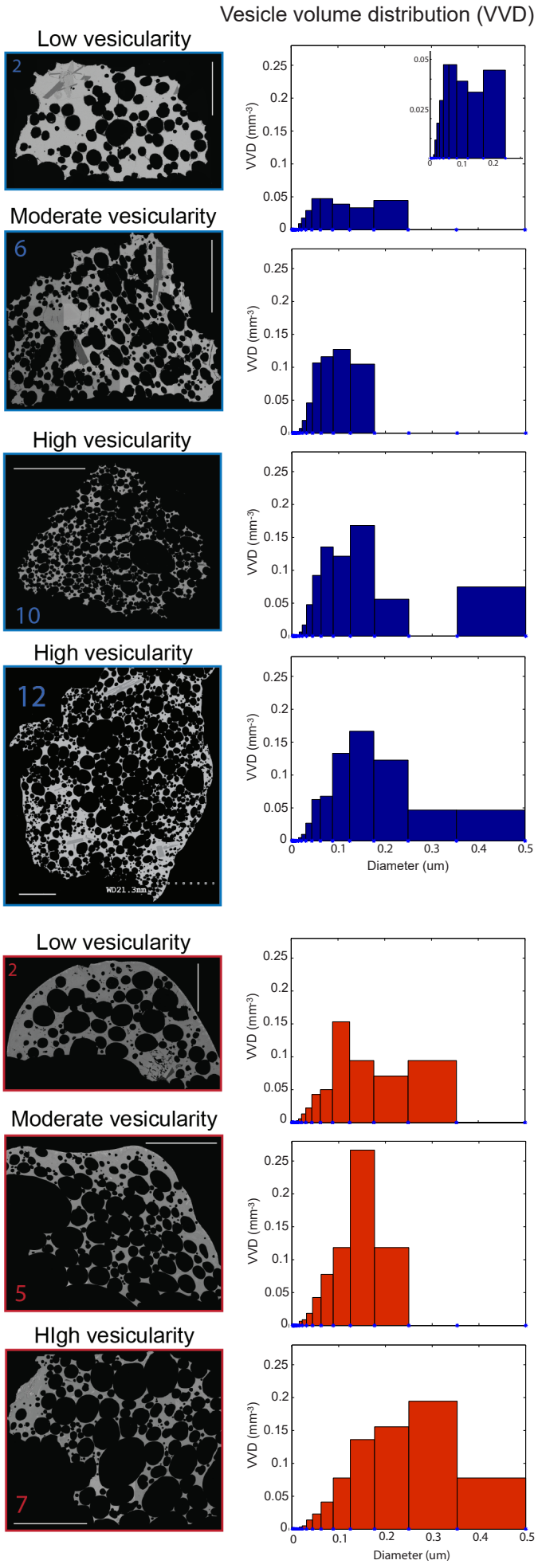
Vesicle volume distribution (VVD)
Low vesicularity
2
Moderate vesicularity
6
High vesicularity
10
High vesicularity
12
WD21.3mm
Low vesicularity
2
Moderate vesicularity
5
HIgh vesicularity
7
VVD (mm-3)
Diameter (um)

Figure 11:

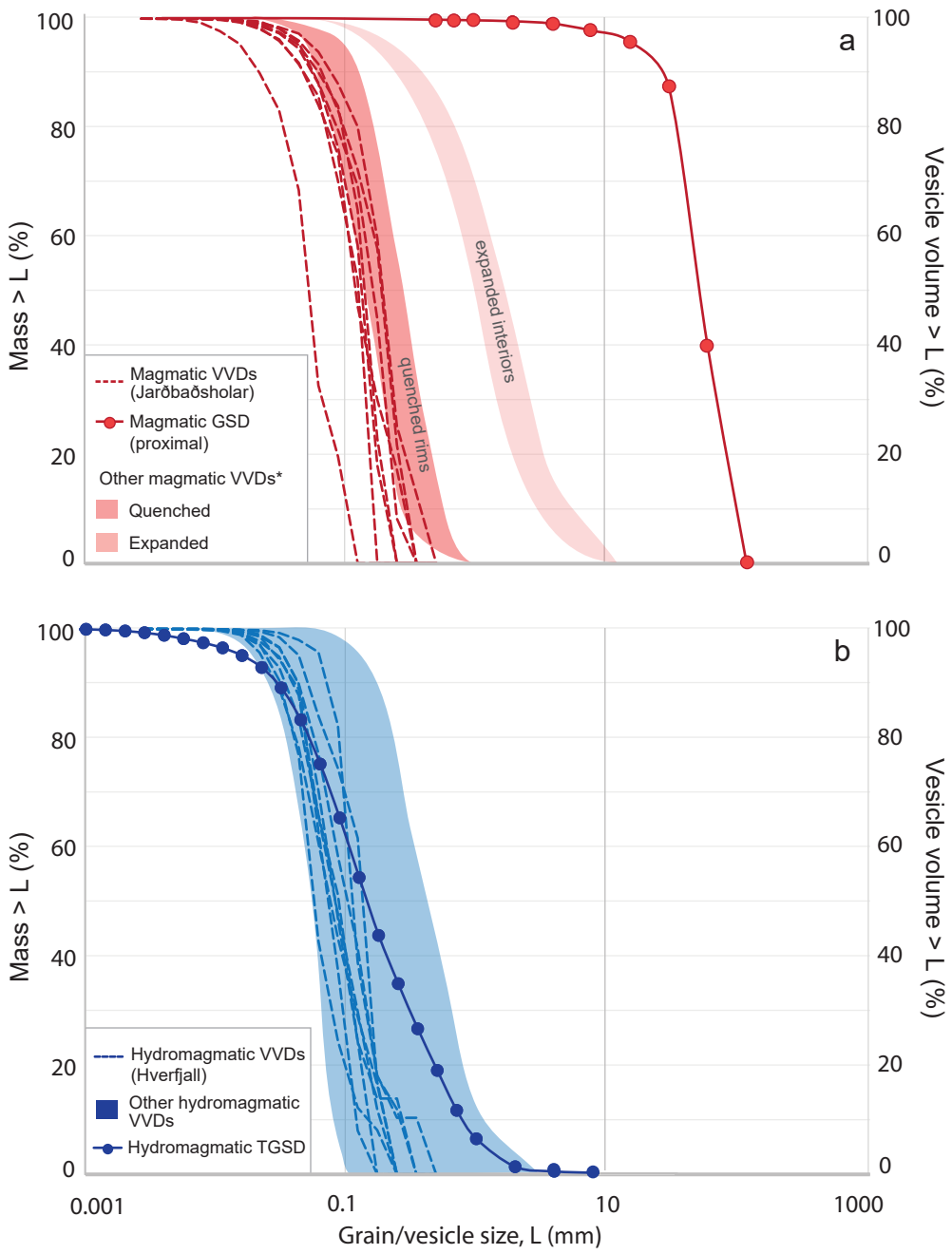
a
b
Mass > L (%)
Vesicle volume > L (%)
Grain/vesicle size, L (mm)
0.001
0.1
10
1000
0
20
40
60
80
100
Magmatic VVDs (Jarðbaðsholar)
Magmatic GSD (proximal)
Other magmatic VVDs*
Quenched
Expanded
quenched rims
expanded interiors
Hydromagmatic VVDs (Hverfjall)
Other hydromagmatic VVDs
Hydromagmatic TGSD

Figure 12:

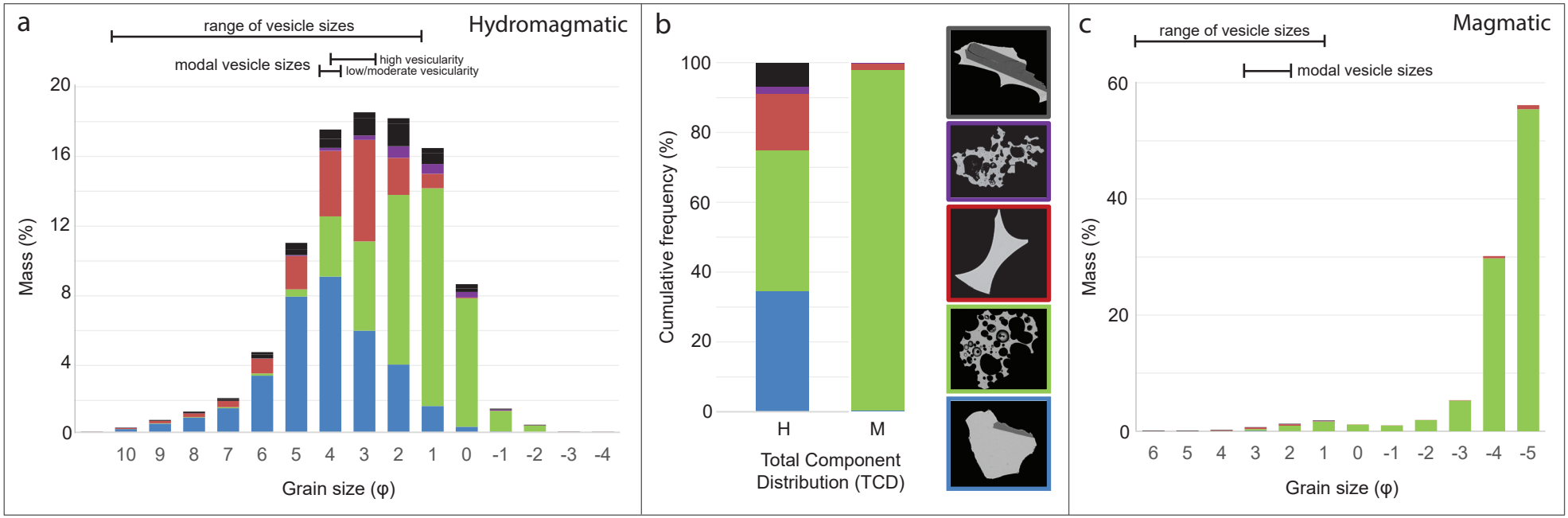
a
range of vesicle sizes
Hydromagmatic
modal vesicle sizes
high vesicularity
low/moderate vesicularity
Mass (%)
Grain size (φ)
b
Cumulative frequency (%)
H
M
Total Component Distribution (TCD)
c
range of vesicle sizes
Magmatic
modal vesicle sizes
Mass (%)
Grain size (φ)

Figure 13:

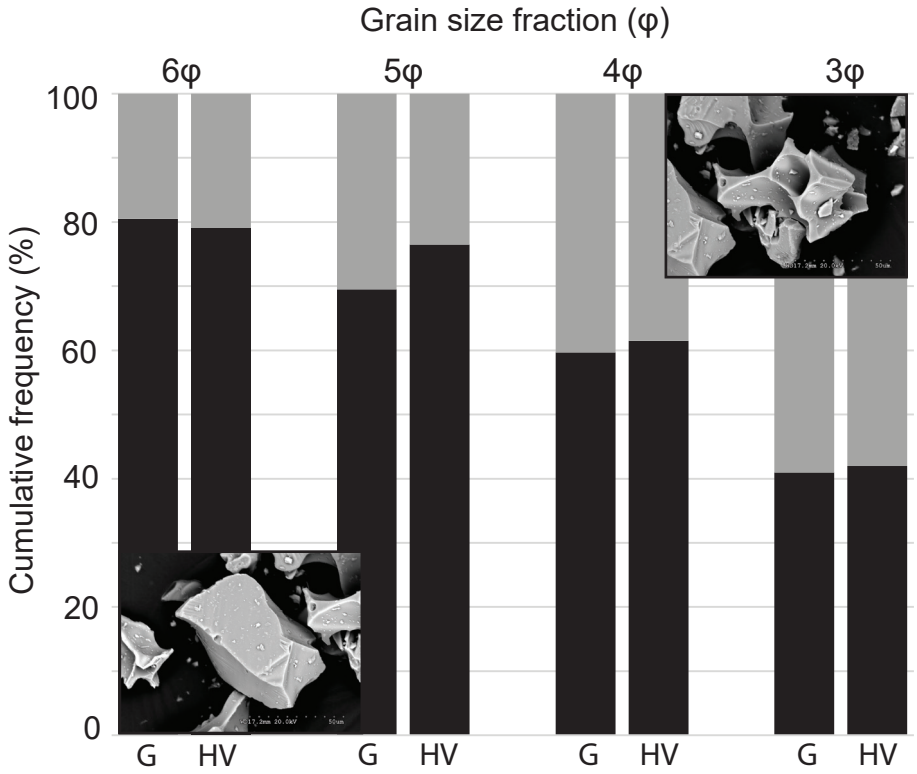
Grain size fraction (φ)
6φ
5φ
4φ
3φ
100
80
60
40
20
0
Cumulative frequency (%)
G
HV
G
HV
G
HV
G
HV

Supplementary Information

Figure S1: Geometric estimation of the volume of the Hverfjall tuff ring edifice. The edifice morphology has been approximated using the volumes of two superposed frustrums. The surface areas of top and basal surfaces, and heights have been measured from GoogleEarth imagery and topographic profiles.

Figure S2: Sensitivity study to determine the minimum sample size for representative componentry measurements. Illustrated example: Hverfjall site 9.3 (2φ); (a) Component proportions for random subsamples, of increasing size, of the total dataset from manual counting (i.e., n=1 to n=600); (b) Variation in the relative standard deviation (RSD) for each component type, as a function of subsample size. The relative standard deviation (RSD) of each individual component falls to <0.5% for sample sizes >200 grains.

Figure S3: Sensitivity study to determine the minimum sample size for clast density distributions; (a) histogram of clast densities for sample site Q1; (b) Variation in the mean density as a function of sample size, from 1 up to the total length of the dataset [n=45]. The mean density stabilises for sample sizes >20 clasts (dotted vertical line).

Figure S4: Sedimentological features of the tuff ring edifice [site 5.11]; (a) Dense lithic bombs define a radial ballistic zone extending ~1.5 km from the centre of the crater; (b) Intra-crater dense lithic ballistics; (c) Alternating ash-rich and lapilli-rich beds on the decimetre-scale; (d) Accretionary pellets and coated particles, comprising lithic or juvenile scoriacious cores surrounded by a fine ash coating; (e) Discontinuous bedding, with anastomosing lapilli lenses;

(f) Small bomb, accompanied by soft sediment deformation of the underlying beds; (g) Lapilli-rich beds, separated by very thin fine ash laminae.

Figure S5: Ballistic modelling using Eject! Software (Mastin, 2001), showing the ballistic range for a clast with diameter of 0.5 m and a density of 2500 kg/m^3 for different combinations of initial velocity and ejection angle. All model input parameters are listed in Table S2.

Figure S6: Sedimentary features of the magmatic deposits; (a) Overview of scoria cone morphology, showing inclined bedding. The locations of sampling sites Q2 and Q3 (Table S1) are annotated; (b) Alternating beds of scoria lapilli and agglutinated spatter [site Q3]; (c) 2.5 m thickness of lava flow overlying hydromagmatic fall and surge units [site 3.8]; (d) Stratigraphic relationships between hydromagmatic surge, magmatic scoria fall and lava flow units [site 3.7].

Figure S7: Grain size characteristics of magmatic (red) and hydromagmatic (blue) fall units (Inman, 1952; Walker, 1971); (a) Median diameter (Mdφ) versus sorting (σ); (b) Sorting versus distance from the vent, either Hverfjall or Jardbadsholar; (c) Median diameter versus distance.

Figure S8: Quantification of vesicle shapes, showing the distribution of form factor values ($FF = \frac{4\pi A}{P^2}$) for measured vesicle populations in the hydromagmatic clasts shown in Figure 1.

Appendix 1 – Volume and Total Grain Size Distribution calculations

Deposit thinning

The existing isopach map is well constrained by 177 thickness measurements that are distributed over proximal to distal regions of the deposit (Saemundsson, 1991; Mattsson and Hoskuldsson, 2011). Figure 4a displays all thickness measurements expressed a function of distance from the centre of the Hverfjall vent. Previous thickness measurements (Saemundsson, 1991; Mattsson and Hoskuldsson, 2011) are shown by the light blue circles on Figure 4a, and exhibit linear thinning behaviour in the medial to distal regions of the deposit. Note the distinct change in slope at ~5 km from the vent. The line of maximum thickness at each distance reflects deposition along the bi-directional NNE-SSW dispersal axes. Many points lie below the maximum thickness at each distance as the deposit is elongated and the isopachs are therefore not radially symmetrical about the vent. Using AshCalc software, we fit the thinning behaviour as (a) a two-segment exponential (Fig. 4b), and (b) a power law (Fig. 4c). The two-segment exponential provides the best fit to the isopach data.

In order to determine the volume of the unconsolidated fall deposits it was necessary to separate out the contribution of the proximal indurated base surge deposits to the total measured thickness. For all outcrops where both fall and surge deposits were exposed together, we recorded the separate thicknesses (Table S1); these data are plotted on Figure 4a as green triangles (surge unit) and blue diamonds (fall unit). The maximum extent of the surge outcrop is approximately 5 km from the centre of the Hverfjall vent in the NNE direction, which corresponds well to the observed change in slope of the total deposit thinning behaviour. Note that the measured thicknesses of most fall exposures directly overlain by surge deposits lie well below the linear thinning trend that characterises the medial to distal part of the deposit, and we therefore infer either that emplacement of the base surges resulted in significant erosion of

the underlying tephra fallout or compaction has occurred due to the weight of the overlying units. However, proximal fall deposit exposures not directly overlain by surges (either because they lie slightly off the axis of surge emplacement, or on elevated ground) have thicknesses that are consistent with the linear thinning trend observed in the medial to distal regions. We conclude that the change in the rate of thinning at ~5 km from the Hverfjall vent is the result of surge emplacement in the proximal regions, and that that fall deposit alone can be characterised by simple exponential thinning within distance (dashed green line; Fig. 4b).

Deposit Volume

The total volume of the deposit was calculated by integrating beneath the two-segment exponential on Figure 4b. The volume of the fall deposit alone was calculated by integrating beneath the single-segment exponential (solid and dashed green line; Fig. 4b), excluding the 50 cm and 100 cm isopachs. Subsets of the fall unit volume contained between pairs of isopachs used for TGSD weighting are shown in Table A1, and are expressed as a proportion of the total deposit volume (fall unit only).

Table A1

Isopach contour (m)	Area (km)	Area$^{1/2}$ (km^3)	Volume (km^3)	Volume (%)
1.0	48.63	6.97		
0.5	29.634	5.44		
0.2	85.672	9.26	0.026	0.33
0.1	212.554	14.58	0.018	0.23
0.05	399.882	20.00	0.013	0.17
0.02	736.198	27.13	0.011	0.14
<0.02			0.011	0.13
Total fall deposit			**0.079**	

Appendix 2 - Stereological methods

Stereology is a statistical technique that determines the 3D distribution of particle sizes within a given volume from a 2D distribution observed in a random cross-section through that volume (Sahagian and Proussevitch, 1998). To test the sensitivity of the final result to the choice of methodology for stereological conversion, we apply four methods to measurements of vesicle area from identical 2D images of three clasts (from the 1–2 mm size fraction of the hydromagmatic fall deposit at site $H_{2.3}$; see Table 1). Acquisition conditions for SEM imaging are detailed in the main text.

As input data, all methods require (a) area measurements of each constituent vesicle, which have been converted into circular equivalent diameters ($EqD = 2\sqrt{\pi A}$); and (b) the total vesicle- and crystal-free melt area. The minimum area cutoff for vesicle measurements was set to 5 μm^2, equivalent to an EqD of 2.5 μm. The first stage of stereological correction is to calculate the number frequency per size class from the EqD values. This is a fundamental step as it requires a decision to be made on how the data are to be binned. Here, we explored three methods of binning: (1) linear (20 μm^2 increments), (2) lognormal (½φ increments), and (3) geometric (logarithmic increments). Next, number frequency data were divided by the total bubble and crystal-free melt area to obtain 2D number densities, N_a (mm^{-2}), for each size class. N_a distributions were converted to 3D number densities, N_v (mm^{-3}), by two methods:

Method 1: 3D number densities, N_v (mm^{-3}), for each size class were calculated by dividing the 2D number density (N_a) by the corresponding linear midpoint diameter for each bubble size class ($N_v = \frac{N_a}{L}$; Underwood, 1970). This technique effectively weights the number of vesicles in each size class by the minimum distance between vesicles of equivalent size to account for decreasing probability of intersecting vesicles of increasing size (Mangan et al., 1993; Klug et al., 2002).

Method 2: For each size class, the 2D number density includes both particles of that size cut through their maximum diameter plus smaller cross-sections through larger particles. The 3D size distribution can therefore be determined iteratively by subtracting from each size class the probabilities of cutting particles from larger size classes in a cross-section equal to the size class being considered (Sahagian and Proussevitch, 1998):

$$N_{Vi} = \frac{1}{H_i}\left(\alpha_i N_{Ai} - \sum_{i-1}^{j=1}(\alpha_{j+1} N_{A(i-j)})\right)$$

where α is a parameter that incorporates the probability of all 2D cross-sections produced by a given particle size (tables of α values are calculated in Sahagian and Proussevitch, 1998), N_{Vi} is the 3D number density of size class *i*, N_{Ai} is the observed 2D number density of size class *i*, and H_i is the mean projected height of the size class *i*. FOAMS is a semi-automated Matlab programme designed to implement stereological conversion by iteration (Shea et al., 2010), and has been used in this study with a minimum bubble diameter of 4 pixels (0.2 μm^2 using our image acquisition parameters).

For both methods, vesicle volume distributions (VVDs) were calculated by multiplying N_v for each size class by the volume of a sphere with a diameter equal to the lower limit of each size class. Note that when the midpoint diameter of the size class was used to calculate the volume of the equivalent sphere, the resulting vesicularities were found to be consistently greater than 1. Random sections through a sphere will result in an average diameter that is 0.85 of the true diameter, resulting in N_v-derived vesicularities that are 10–20% lower than the true vesicularity (e.g., Cashman and Marsh, 1988; Mangan et al., 1993; Klug et al., 2002). To correct for this cut effect, a correction factor was determined by dividing the N_v-derived vesicularity (calculated by summing the N_v values over all size classes) by the 2D image vesicularity,

assuming that the 2D vesicularity is representative of the 3D vesicularity through which it is a cross-section. To obtain the final N_v and volume distributions, 3D number densities across all size classes were multiplied by the correction factor, and the VVD recalculated. Note that some of the highest vesicularity pyroclasts had N_v-derived vesicularities greater than the 2D image vesicularity due to the influence of a few large vesicles (which contribute disproportionately to the total volume) and therefore required correction factors <1. Total bubble number densities, BNDs (mm^3) were calculated by summing N_v values across all size classes >8 μm (following Murtagh and White, 2013).

Results

All four methods of stereological conversion (Method 1: linear, lognormal and geometric binning; Method 2: geometric binning) yield similar results for identical datasets of N_a values. Cumulative VSDs (Log N_v > L vs. Log L) have similar shapes that overlap closely (Figs. B1, B2, B3); however, it is clear that the use of linear bins limits the information on how the smallest bubbles are distributed. When cumulative volume fraction is plotted against L, the four distributions overlap almost exactly, indicating that the contribution of each vesicle size to the overall vesicularity is similar regardless of the method used (Fig. B4). Graphically, VVDs are broadly similar in shape with comparable modal bubble sizes; however, some offset in the modal size class can result from differences in the placement of size class boundaries between the different binning styles, particularly when linear bins are used (Figs. B1, B2, B3). Nevertheless, when the VVDs from Method 1 and 2 (both using the same geometric binning scale) are compared, distribution shapes and modal size classes are in close agreement.

Conclusion

This sensitivity study has shown that the 3D number and volume distributions are largely independent of the stereological conversion method used, consistent with a similar comparison made by Klug et al., (2002). **Method 1, with lognormal binning,** has therefore been chosen based on practical considerations. Method 1 is preferred over Method 2, as it requires significantly less handling of 2D data (and is therefore a more transparent process) and offers greater flexibility in the definition of vesicle size ranges (Klug et al., 2002). As bubble diameters are distributed over several orders of magnitude, lognormal or geometric bins are preferred over linear bins; linear binning not only obscures information on the smallest bubble sizes, but can also introduce spurious additional modes and/or gaps in the distribution. Lastly, the use of lognormal (φ) instead of geometric, bins makes it easier to compare textural distributions with other ash properties (e.g., shape and density) that have also been measured on sieved φ-size classes. Note that the close similarity in the results obtained by the two methods may be in part due to the highly spherical nature of the bubbles in the Hverfjall pyroclasts used in this sensitivity study. We speculate that the discrepancies between different techniques may become more apparent as bubbles deviate from spherical.

Additional references for supplementary information

Cashman, K.V. and Marsh, B.D., 1988. Crystal size distribution (CSD) in rocks and the kinetics and dynamics of crystallization II: Makaopuhi lava lake. Contributions to Mineralogy and Petrology, 99(3), 292-305.

Inman, D.L., 1952. Measures for describing the size distribution of sediments. Journal of Sedimentary Research, 22(3).

Klug, C., Cashman, K. and Bacon, C., 2002. Structure and physical characteristics of pumice from the climactic eruption of Mount Mazama (Crater Lake), Oregon. Bulletin of Volcanology, 64, 486-501.

Mangan, M.T., Cashman, K.V. and Newman, S., 1993. Vesiculation of basaltic magma during eruption. Geology, 21, 157-160.

Sahagian, D.L. and Proussevitch, A.A., 1998. 3D particle size distributions from 2D observations: Stereology for natural applications. Journal of Volcanology and Geothermal Research, 84(3), 73-196.

Underwood, E.E., 1970. Quantitative stereology.

Walker, G.P., 1971. Grain-size characteristics of pyroclastic deposits. The Journal of Geology, 79(6), pp.696-714.

Figure B1: Sensitivity test - hydromagmatic clast B

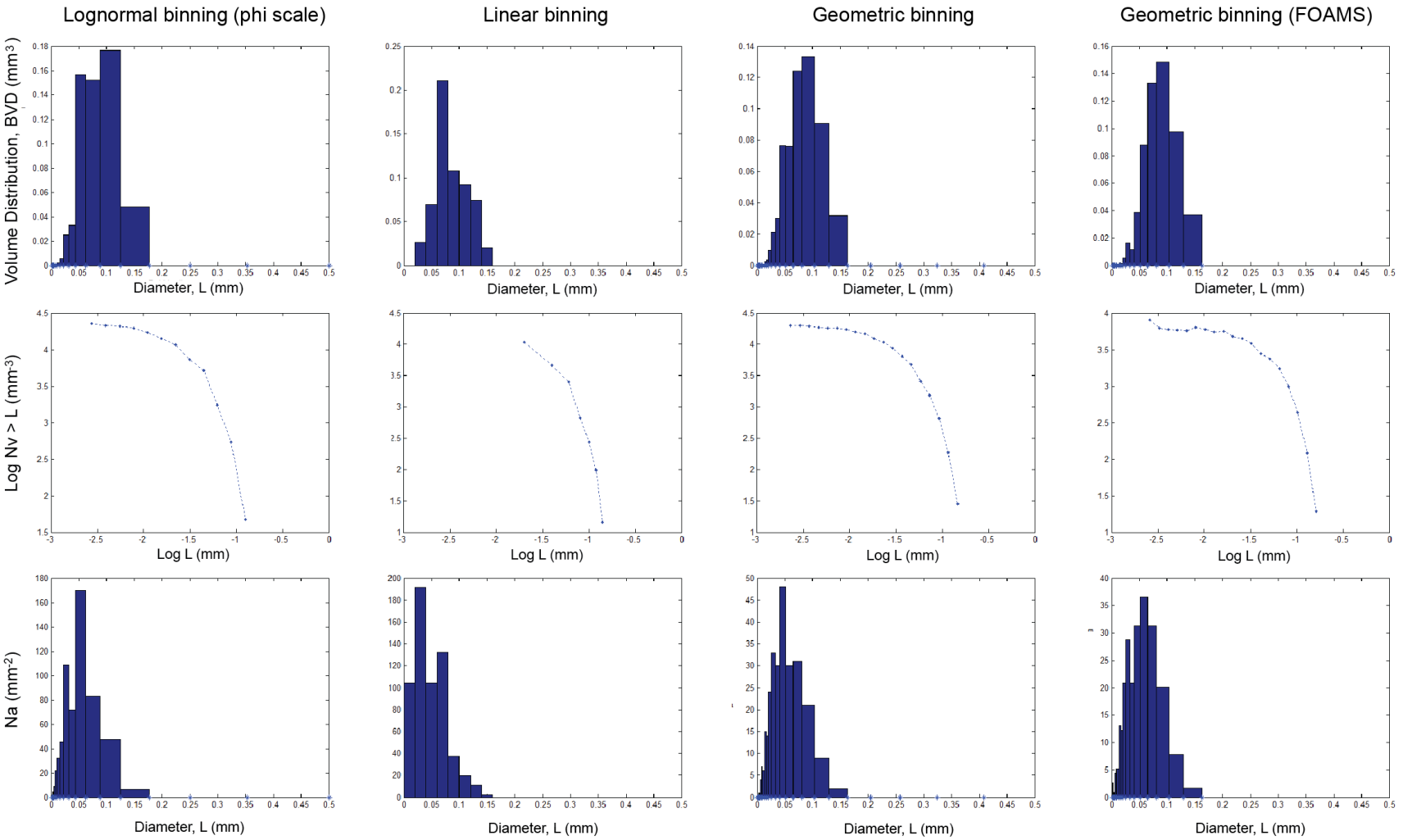

Figure B2: Sensitivity test - hydromagmatic clast E

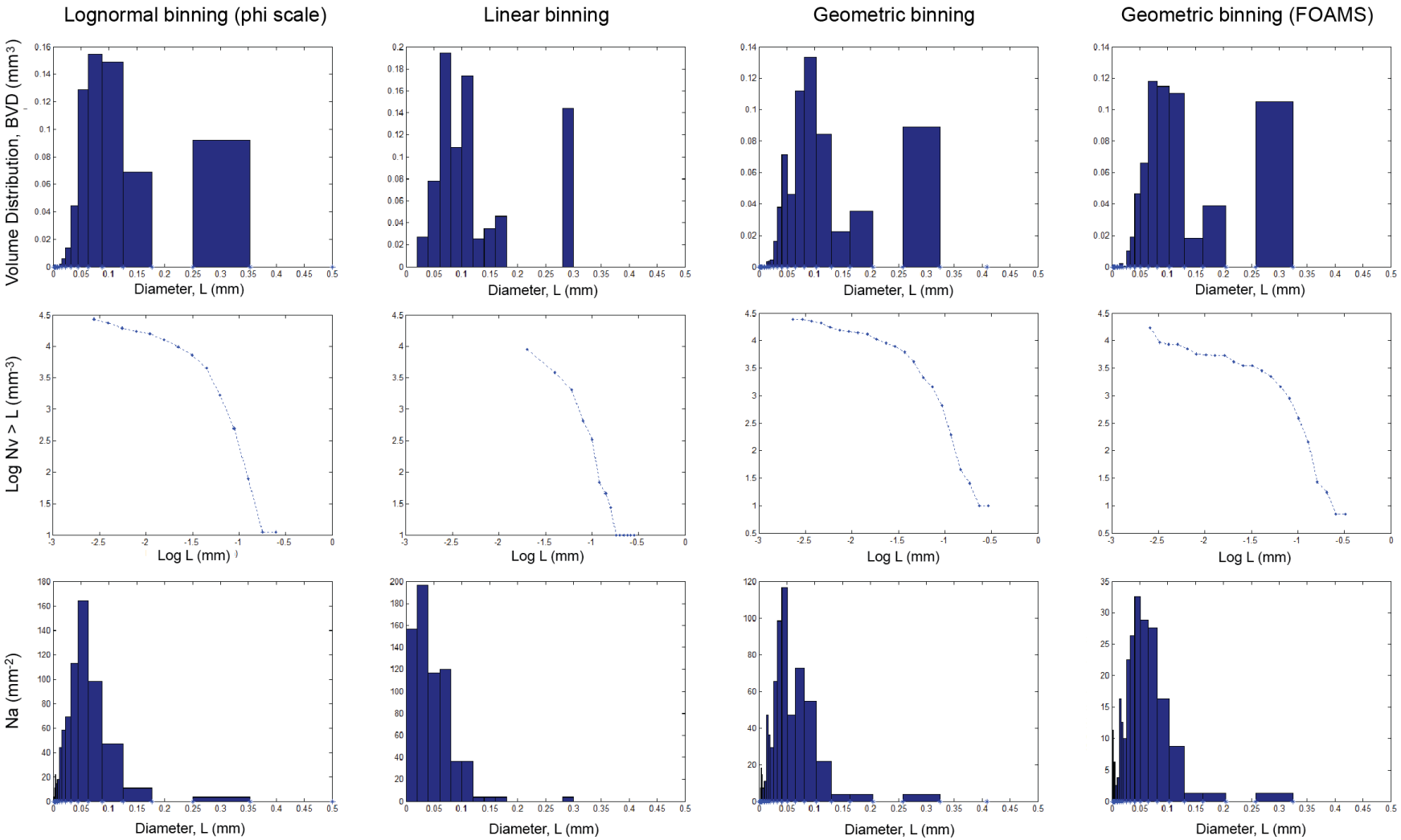

Figure B3: Sensitivity test - hydromagmatic clast A

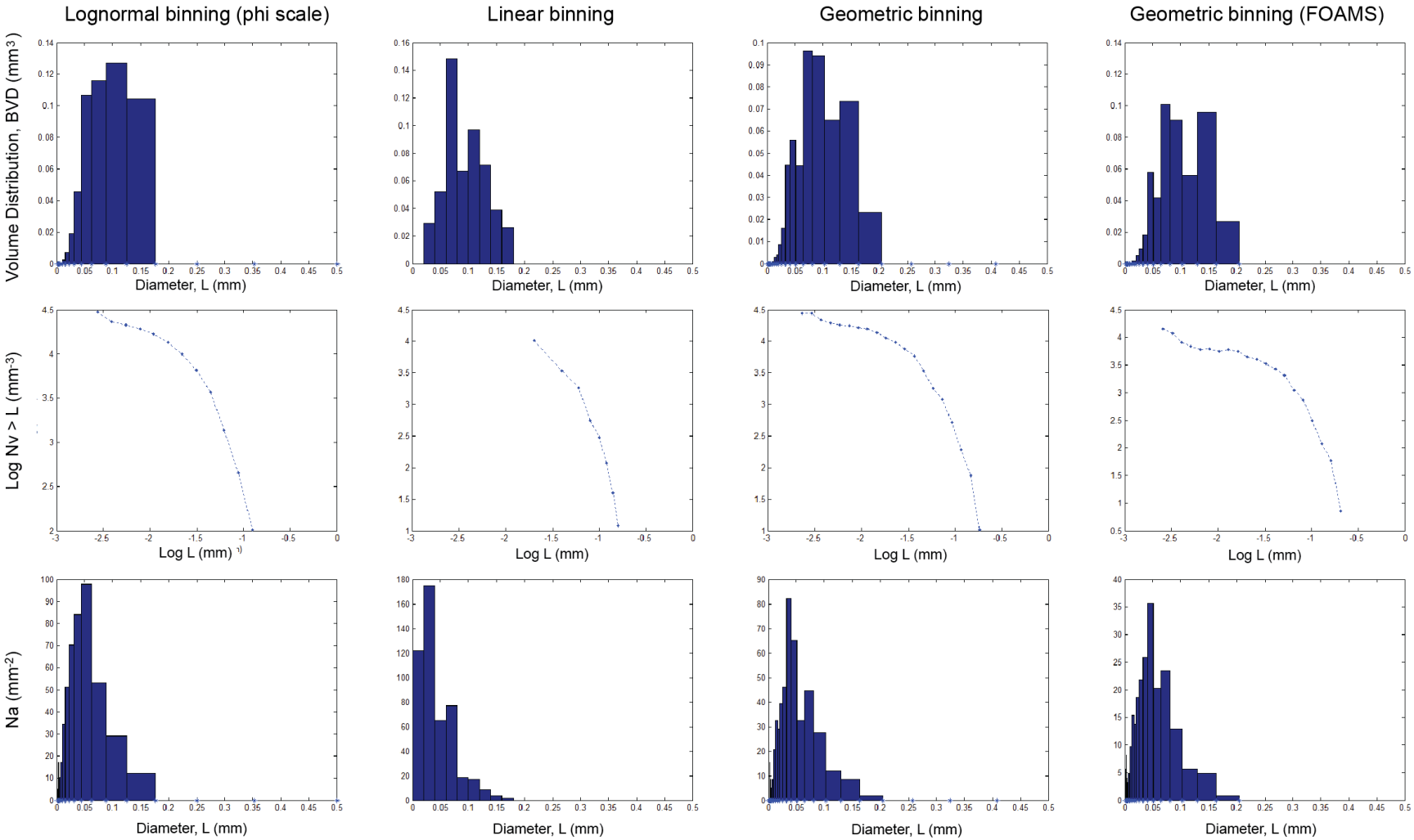

Figure: B4: Cumulative volume fraction (%) for hydromagmatic clasts from the 1-2 mm size fraction of sample H1.5 (a) Clast B; (B) Clast E; and (c) Clast A.

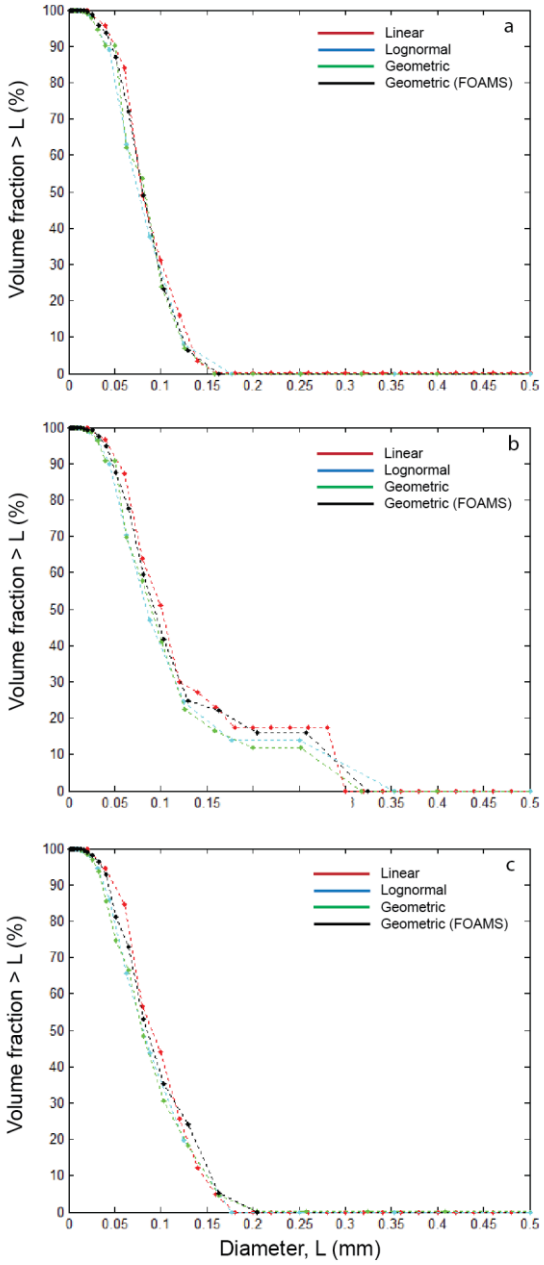

Table S1: Summary of the morphological properties of hydromagmatic landforms

Landform	Morphology	Deposits	Examples
Tuff cones	Steep-sided, with high slope angles and large aspect ratios (height/crater diameter)	Consolidated tephra fallout beds that rarely extend more than one crater diameter away from the crater rim. Cone edifices generally comprise from poorly-sorted lapilli tuffs, with sedimentological features indicative of water-saturated emplacement of cohesive sediment	*Surtsey, Iceland* (shallow marine; Wohletz and Sheridan, 1983). *Diamond Head and Koko Crater, Hawaii* (seawater intruding highly permeable hard rocks; Wohletz and Sheridan, 1983). *Ilchulbong, Korea* (seawater intruding highly permeable lavas; Murtagh et al., 2011). *Ambae, Vanuatu* (shallow lacustrine; Nemeth et al., 2006).
Tuff rings	Shallow topographic profiles, with gently-dipping beds and low aspect ratios	Extensive distal deposits dominated (at least proximally) by energetic base surge flows. Individual base surges range in character from well stratified 'dry' tuffs to poorly-sorted water-saturated lapilli-tuffs, where water was present on deposition as superheated steam or condensed liquid water, respectively (Wohletz and Sheridan, 1983; Chough and Sohn, 1990)	*Ohakune, New Zealand* (groundwater within laharic deposits; Houghton and Hackett, 1983). *Songaksan and Suwolbong, Korea* (groundwater within basalt lavas; Sohn, 1996; Chough and Sohn, 1996; Sohn and Park, 2005). *Taal, Philippines* (intra-lacustrine island; Moore, 1967; White and Ross, 2011).

Table S2: Sampling locations and deposit thickness measurements. GPS coordinates are given in the UTM system WGS 64, Zone 28W.

Field Location	Latitude	Longitude	Hydro-magmatic fall (cm)	Hydro-magmatic surge (cm)	Scoria fall (cm)	Lava flow (cm)	Distance from vent (km)	Grain size distribution measured?
1.2	65 37 46.6 N	16 51 00.7 W	1	50	0	0	3.09	
2.2	65 38 51.5 N	16 49 07.5 W	0.5	27	0	0	5.58	x
2.7	65 38 55.0 N	16 48 56.5 W	3	30	0	0	5.69	x
2.4	65 39 02.0 N	16 49 08.5 W	remobilised	0	0	0	5.79	
2.5	65 38 38.3 N	16 49 18.2 W	1.5	0	0	0	5.07	x
2.6	65 38 48.5 N	16 49 25.7 W	4	4.5	0	0	5.36	x
3.2	65 38 29.1 N	16 50 04.3 W	0	250	0	0	4.64	
3.3	65 37 56.4 N	16 50 39.1 W	10	8	0	0	3.46	x
3.5	65 37 58.1 N	16 50 37.4 W	3	20	20	150	3.52	
3.7	65 37 59.9 N	16 50 32.9 W	0	75	15	70	3.61	x
3.8	65 38 08.0 N	16 50 30.9 W	2	NR	4	250	3.82	
3.9	65 38 08.4 N	16 50 08.6 W	0	60	0	0	3.98	
3.9b	65 38 01.3 N	16 50 04.7 W	0	80	0	0	3.81	
3.10	65 37 57.2 N	16 50 08.1 W	0	75	20	0	3.69	x
4.1	65 37 50.5 N	16 51 01.7 W	1	60	Interbedded	0	3.14	
4.4	65 36 58.4 N	16 50 58.0 W	0	800	0	0	1.75	
4.5	65 36 53.4 N	16 50 48.9 W	0	700	0	0	1.74	
4.6	65 37 04.7 N	16 50 53.6 W	1	200	0	0	1.98	
4.7	65 37 04.1 N	16 51 07.5 W	1	170	0	0	1.85	
5.1	65 36 50.6 N	16 51 01.0 W	0	90	0	0	1.59	
5.2	65 36 49.8 N	16 50 53.6 W	0	>600	0	0	1.61	
5.3	65 37 12.4 N	16 51 38.6 W	0	50	0	0	1.92	
5.4	65 37 15.6 N	16 51 41.1 W	0	58	0	0	1.98	
5.8	65 37 00.0 N	16 51 42.9 W	0	55	0	0	1.53	

5.11	65 36 30.3 N	16 52 44.9 W	0	8750	0	0	0.56	
6.1	65 40 51.9 N	16 32 59.9 W	4	0	0	0	17.25	
6.2	65 41 47.5 N	16 32 33.7 W	3	0	0	0	18.42	x
6.4	65 42 53.6 N	16 32 13.6 W	3	0	0	0	19.84	x
6.5	65 38 28.8 N	16 48 41.2 W	3	85	0	0	5.06	
6.6	65 38 07.1 N	16 48 47.7 W	4	72	0	0	4.52	x
7.2	65 39 19.4 N	16 52 05.1 W	2	0	0	0	5.76	x
7.3	65 38 59.9 N	16 52 04.1 W	5.5	0	0	0	5.15	
7.4	65 38 53.3 N	16 52 09.6 W	16.5	0	2	0	4.95	x
7.5	65 39 25.6 N	16 34 02.0 W	22	0	0	0	15.33	x
7.7	65 38 00.5 N	16 50 57.2 W	0	120	0	0	3.49	
7.8	65 38 00.0 N	16 51 25.6 W	0	175	Interbedded	0	3.39	
8.2	65 38 01.4 N	16 51 41.7 W	0	42	>300	0	3.36	
8.3	65 38 17.9 N	16 51 57.5 W	0	20	0	0	3.90	
8.4	65 33 52.4 N	17 06 29.6 W	5	0	0	0	11.66	x
8.5	65 32 37.9 N	17 05 58.2 W	1	0	0	0	12.38	x
2.3	65 35 39.6 N	16 51 38.3 W	30	0	0	0	1.30	x
6.3	65 37 57.4 N	16 50 38.0 W	24	90	40	0	3.47	x
9.3	65 38 36.1 N	16 52 17.6 W	24.5	0	2.5	0	4.30	x
8.9	65 37 00.9 N	16 51 27.6 W	<1	348	0	0	1.62	
Q1	65 37 55.2 N	16 50 59.4 W	0	80	>500	0	0.42	
Q2	65 38 16.3 N	16 51 13.6 W	0	40	>500	0	0.25	x
Q3	65 38 13.8 N	16 51 11.8 W	0	0	>500	0	0.18	x
5.0	65 38 39.9 N	16 53 44.6 W	12.5	0	0	0	4.59	
8.6	65 37 20.2 N	16 51 23.5 W	0	102	0	0	2.17	
1.1	65 33 52.2 N	16 51 20.9 W	21	0	0	0	4.54	x

Table S3: Input parameters for ballistic modelling in Eject! (Mastin, 2001)

Parameter	**Value**
Drag Coefficient (constant)	1
Shape	Sphere
Density (kg/m3)	2500
Clast diameter (m)	0.5
Tailwind (m/s)	0
Thermal lapse rate (˚C)	6.5
T (˚C) at sea level	10
Take-off elevation (m)	335
Change in elevation (m)	-28
Zone of reduced drag (m)	400
Range of ejection angles (˚)	30–60
Range of velocities (m/s)	80–160

Table S4: Grain size distributions. All sieve data contained in supplementary Excel file.

Table S5: Summary of componentry proportions as a function of grain size and dispersal distance. Data collected by manual counting from backscattered electron SEM images.

Sample	Grain size (ϕ)	Grain size (μm)	Dense	Vesicular	Shards	Micro-crystalline	Crystal fragments	Holocrystalline lithics
$H_{2.3}$	6	16	63.5	2.0	27.2	0.0	4.5	2.8
$H_{9.3}$	6	16	70.9	5.6	14.6	0.0	5.4	3.4
$H_{6.3}$	6	16	75.4	2.2	14.1	0.0	4.6	3.8
$H_{7.5}$	6	16	72.4	1.5	18.0	0.6	6.2	1.2
$H_{2.3}$	5	32	65.5	0.0	26.0	0.0	4.5	4.0
$H_{9.3}$	5	32	76.4	4.8	10.6	1.1	3.4	3.7
$H_{6.3}$	5	32	75.9	4.3	15.2	0.3	2.2	2.2
$H_{7.5}$	5	32	69.8	3.9	20.0	0.0	2.6	3.6
$H_{2.3}$	4	63	44.9	19.8	23.1	2.0	5.3	4.9
$H_{9.3}$	4	63	53.2	25.5	15.1	0.0	4.3	1.8
$H_{6.3}$	4	63	55.5	13.0	27.6	0.0	1.7	2.2
$H_{7.5}$	4	63	52.1	21.2	20.7	1.8	0.5	3.7
$H_{2.3}$	3	125	31.1	18.7	36.3	0.5	9.3	4.1
$H_{9.3}$	3	125	35.3	33.1	28.2	1.2	2.7	0.5
$H_{6.3}$	3	125	27.4	35.5	31.7	0.5	4.3	0.5

$H_{7.5}$	3	125	33.6	24.5	31.1	3.3	5.0	2.5
$H_{2.3}$	2	250	17.3	54.7	8.2	2.1	16.0	1.6
$H_{9.3}$	2	250	27.2	52.7	8.2	5.8	3.2	1.0
$H_{6.3}$	2	250	20.3	57.1	14.7	2.8	3.4	1.7
$H_{7.5}$	2	250	21.0	50.5	16.0	4.0	5.5	3.0
$H_{2.3}$	1	500	5.3	82.4	2.7	1.6	6.4	1.6
$H_{9.3}$	1	500	10.0	75.9	5.3	6.5	1.2	1.2
$H_{6.3}$	1	500	11.9	76.7	4.7	2.6	3.6	0.5
$H_{7.5}$	1	500	9.8	71.5	7.8	3.1	3.6	4.1
$H_{2.3}$	0	1000	5.8	79.1	0.7	7.2	2.9	4.3
$H_{9.3}$	0	1000	3.8	87.6	0.0	2.9	2.9	2.9
$H_{6.3}$	0	1000	1.7	93.8	0.6	1.1	1.1	1.7
M_{Q1}	4	63	22.6	11.8	59.2	3.1	2.1	1.0
$M_{6.3}$	4	63	27.2	12.9	50.9	2.2	1.3	5.4
M_{Q1}	3	125	9.9	39.2	44.1	2.3	4.5	0.0
$M_{6.3}$	3	125	15.9	45.8	35.7	0.0	2.6	0.0
M_{Q1}	2	250	3.7	69.5	18.2	5.9	2.1	0.5
$M_{6.3}$	2	250	3.0	74.9	20.1	0.0	2.0	0.0
M_{Q1}	1	500	0.7	83.1	4.9	6.3	4.9	0.0
$M_{6.3}$	1	500	1.3	95.6	0.0	0.6	2.5	0.0
M_{Q1}	0	1000	0.0	97.4	2.6	0.0	0.0	0.0
$M_{6.3}$	0	1000	0.0	100.0	0.0	0.0	0.0	0.0

Table S6: Summary of clast textural properties

Clast Number	Grain size (mm)	Bubble-free melt area (mm^2)	Crystal area (mm^2)	Bubble and crystal-free melt area (mm^2)	Total particle area (mm^2)	2D Image Vesicularity	Number density, BND (x 10^{13} m^{-3})	Modal size class (μm; by volume)
Hydromagmatic								
1	1 - 2	0.757	0.000	0.757	1.016	0.25	0.15	-
2	1 - 2	1.250	0.035	1.215	1.673	0.27	1.32	45-91
3	1 - 2	0.974	0.018	0.956	1.551	0.38	0.3	91-125
4	1 - 2	0.517	0.048	0.469	0.822	0.43	2	45-180
5	1 - 2	0.539	0.040	0.499	0.967	0.48	2.53	45-63
6	1 - 2	0.609	0.026	0.583	1.235	0.53	2.28	91-125
7	1 - 2	0.485	0.025	0.460	1.158	0.60	1.95	91-125
8	1 - 2	0.330	0.007	0.323	0.891	0.64	1.92	91-125
9	1 - 2	0.292	0.018	0.274	0.798	0.66	1.75	63-91
10	1 - 2	0.538	0.000	0.538	1.919	0.72	1.42	125-180
11	1 - 2	0.280	0.000	0.280	1.116	0.75	0.96	125-180
12	4 - 8	1.860	0.059	1.801	5.891	0.69	1.19	125-180
Magmatic								
1	1 - 2	0.396	0.041	0.355	0.759	0.53	1.44	125-180
2	1 - 2	0.644	0.000	0.644	1.448	0.55	1.35	91-125
3	1 - 2	0.649	0.000	0.649	1.637	0.60	0.83	180-250
4	1 - 2	0.467	0.000	0.467	1.312	0.64	0.77	180-250
5	1 - 2	0.402	0.000	0.402	1.186	0.66	1.31	125-180
6	1 - 2	0.364	0.004	0.360	1.228	0.71	1.28	125-180
7	1 - 2	0.462	0.000	0.462	1.729	0.73	0.73	250-355
8	1 - 2	0.292	0.000	0.292	1.144	0.74	0.95	180-250
9	16 - 32	1.325	0.022	1.303	1.990	0.35	2.17	45-125